J. Fluid Mech. (2016), *vol.* 792, *pp.* 470–498.
doi:10.1017/jfm.2016.47

A numerical investigation of the wake of an axisymmetric body with appendages

A. Posa[1] **and E. Balaras**[1,†]

[1]Department of Mechanical and Aerospace Engineering, The George Washington University, 800 22nd Street NW, Washington, DC 20052, USA

(Received 28 April 2015; revised 4 November 2015; accepted 12 January 2016; first published online 3 March 2016)

We report wall-resolved large-eddy simulations of an axisymmetric body of revolution with appendages. The geometry is that of the DARPA SUBOFF body at 0 yaw angle and a Reynolds number equal to $Re_L = 1.2 \times 10^6$ (based on the free-stream velocity and the length of the body). The computational grid, composed of approximately 3 billion nodes, is designed to capture all essential flow features, including the turbulent boundary layers on the surface of the body. Our results are in good agreement with measurements available in the literature. It is shown that the wake of the body is affected mainly by the shear layer from the trailing edge of the fins and the turbulent boundary layer growing along the stern, while the influence of the wake of the sail is minimal. In agreement with the reference experiments, a bimodal behaviour for the turbulent stresses is observed in the wake. This is due to the displacement of the maximum of turbulent kinetic energy away from the wall along the surface of the stern, where the boundary layer is subjected to strong adverse pressure gradients. The junction flows, produced by the interaction of the boundary layer with the leading edge of the fins, enhance this bimodal pattern, feeding additional turbulence in the boundary layer and the downstream wake. The evolution of the wake towards self-similarity is also investigated up to nine diameters downstream of the tail. We found the mean flow approaches this condition, while its development is delayed by the wake of the appendages, especially by the flow coming from the tip of the fins. However, the width of the wake and its maximum momentum deficit follow the expected power-law behaviour on the side away from the sail. The second-order statistics, on the other hand, are still far from self-similarity, which is consistent with experimental observations in the literature.

Key words: turbulence simulation, turbulent boundary layers, wakes

1. Introduction

Wake flows are of interest in a variety of technological applications. Wakes are produced by airplanes, ships, submarines and any kind of surface vehicle. In general, their study is very demanding both computationally and experimentally, due to their long development. Computationally this means that one needs to extend the computational box keeping a high level of numerical resolution far from the

†Email address for correspondence: balaras@gwu.edu

wake-producing body. Also, as the intensity of the velocity fluctuations decreases with the distance from the body, experimental measurements become more challenging. From a computational standpoint an additional challenge is the need to accurately resolve the thin boundary layers on the surface of the wake generator, especially when the flow problem involves high Reynolds numbers and complex geometries.

In the present work we will focus on the wake of an idealized submarine geometry, which is an axisymmetric body with appendages. Jiménez, Hultmark & Smits (2010*a*) and Jiménez, Reynolds & Smits (2010*b*) conducted experiments in the wake of the same body, with and without appendages. In both cases the axial symmetry was actually broken by the support, which mimicked a semi-infinite sail. In the latter case they considered Reynolds numbers, based on the free-stream velocity, U_∞, and the length of the model, L, in the range of $1.1 \times 10^6 < Re_L < 67 \times 10^6$, focusing on the self-similar development of the wake, up to 15 diameters from the tail of the body. They showed that the similarity velocity and length scales evolved in the wake according to the expected power laws. They also verified the actual development of a self-similar condition for the first-order statistics, while the second-order statistics were not yet self-similar up to 15 diameters from the tail. The influence of the support was also studied and they reported a significant effect on the statistics of the intermediate wake on the side where it was located. Jiménez *et al.* (2010*b*) studied the effect of additional appendages (four fins on the stern) on the intermediate wake in a narrower range of Reynolds numbers ($4.9 \times 10^5 < Re_L < 1.8 \times 10^6$). They found a decreased mean velocity at the locations directly downstream of their tips and increased turbulence intensities, with a stronger bimodal behaviour in the cross-stream profiles of the normal stresses. More complex profiles of the shear stress were also observed and were attributed to the junction flows produced by the additional fins.

Both the above experiments point to the complexity of the near wake, especially for the case of the appended body, which appears to be influenced by various competing effects, such as stern boundary layers, shear layers and junction flows originating from the sail and appendages, etc. Assessing the impact of each of these features on the overall wake evolution experimentally is very challenging. High-fidelity, predictive computational tools, such as the large-eddy simulation (LES) approach, can greatly enhance our understanding of these complex problems. As of today, however, due to cost considerations the majority of the earlier works utilized Reynolds-averaged Navier–Stokes (RANS) formulations, while the boundary layers on the wake-producing body were modelled using wall functions (Givler *et al.* 1991) or thin-layer approximations (Taylor *et al.* 1998). In a more recent study by Boger & Dreyer (2006) an overset grid methodology was used to fully resolve the boundary layers within a RANS formulation. They reported axial symmetric and three-dimensional simulations. Although no results were provided in the turbulent boundary layer region, the comparison of the integral forces and moments to experiments was satisfactory. Phillips, Turnock & Furlong (2010) utilized RANS to simulate the flow around an axial symmetric submarine body in drift conditions (angle of 15°) at $Re_L = 1.1 \times 10^7$. By comparison with experiments in the literature they verified that in such configurations, where separation occurs, the results strongly depend on the adopted turbulence model.

In more recent computational studies more emphasis is placed on utilizing hybrid formulations such as the detached eddy simulation (DES) approach. Alin *et al.* (2010), for example, presented RANS, LES and DES results for the DARPA SUBOFF (DSub) model at $Re_L = 1.2 \times 10^7$. For both RANS and LES computations the wall-layer was modelled. Results were in better agreement with experiments in the literature for LES

and DES. The pressure coefficient was accurately predicted, while the skin-friction coefficient was underestimated. A DES study has also been reported by Zhihua, Ying & Chengxu (2011, 2012), where they considered the DSub geometry and compared their results to the experiments by Huang *et al.* (1994). Similar studies for the DSub geometry have been carried out by Vaz, Toxopeus & Holmes (2010), Chase & Carrica (2013) and Chase, Michael & Carrica (2013), who performed both RANS and DDES (delayed detached eddy simulation by Spalart *et al.* (2006)) computations. DES and hybrid RANS/implicit LES approaches, coupled with wall-functions formulations, were adopted by Bhushan, Alam & Walters (2013) to simulate the appended DSub. As with earlier studies the adoption of a LES modelling strategy in the wake improved the results. The use of lower-order closures (i.e. RANS) to predict the flow over the wake-producing body is problematic due to the complex dynamic interactions between boundary layers, shear layers and junction flows.

To address these issues, in the present work we report wall-resolved LES for the case of an appended DSub model at flow conditions that match those in the experiment by Jiménez *et al.* (2010*b*). The level of numerical resolution utilized in the present computations goes beyond what has been reported in the literature today, resolving all essential flow features, including also the turbulent boundary layer on the surface of the body. The resulting database will enable us to explore the details of the interaction of the boundary layers, junction and tip flows on the body with the near and intermediate wake. We will further investigate some of the conjectures outlined by Jiménez *et al.* (2010*a*,*b*) and will also identify the effects of the semi-infinite sail that is used in the experiments to support the model. Furthermore, the evolution of the wake towards self-similarity and the impact of the appendages will be explored.

This paper is organized as follows. First the methodologies and computational set-up are given in § 2. Then the results are presented in § 3, where a general overview of the flow (§ 3.1), the statistics in the turbulent boundary layer (§ 3.2), a comparison with the experiments (§ 3.3), the bimodal distribution in the wake (§ 3.4) and the evolution downstream towards self-similarity (§ 3.5) are discussed. Finally, the conclusions of the present study are reported in § 4.

2. Methodologies and computational set-up

In the LES reported here, the filtered Navier–Stokes equations for incompressible flows are solved:

$$\frac{\partial \tilde{u}_i}{\partial x_i} = 0 \tag{2.1}$$

$$\frac{\partial \tilde{u}_i}{\partial t} + \frac{\partial \tilde{u}_i \tilde{u}_j}{\partial x_j} = -\frac{\partial \tilde{p}}{\partial x_i} - \frac{\partial \tau_{ij}}{\partial x_j} + \frac{1}{Re}\frac{\partial^2 \tilde{u}_i}{\partial x_j x_j} + f_i, \tag{2.2}$$

where $\tilde{u}$ and $\tilde{p}$ are the filtered velocity and pressure, $Re = UL/\nu$ is the Reynolds number (U and L being a reference velocity and length scales, and ν the kinematic viscosity of the fluid), f_i is a forcing term that will be discussed below. Spatial and time coordinates are denoted by x and t, respectively. The effect of the scales smaller than the filter size is introduced through the SGS tensor $\tau_{ij} = \widetilde{u_i u_j} - \tilde{u}_i \tilde{u}_j$. In all computations reported in this study the wall-adapting local eddy-viscosity (WALE) model (Nicoud & Ducros 1999) is utilized. We have found that the model exhibits the correct limiting behaviour near the wall and the eddy viscosity vanishes in laminar regions. For the particular flow configuration we found the WALE model to be as

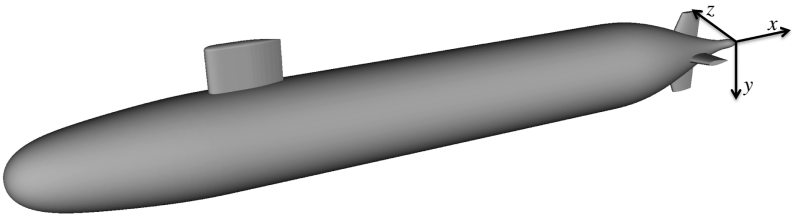

FIGURE 1. Simulated geometry of the DARPA SUBOFF developed by Groves, Huang & Chang (1989).

accurate as the family of dynamic models (i.e. the Lagrangian dynamic model by Meneveau, Lund & Cabot (1996)) at a lower computational cost. We should also note that in the computations reported below the ratio between eddy and molecular viscosity, ν_t/ν, in the wake was always less than one. The eddy-viscosity was higher only in the near wake of the sail, and at the trailing edge of the fins, where $\nu_t/\nu < 5$.

The governing equations are solved on a staggered grid in cylindrical coordinates. The singularity at the axis is addressed by treating the radial component of the momentum equation as a radial flux, which is equal to 0 for $r = 0$. The use of a staggered grid was also helpful in decreasing the number of singularities, since the azimuthal and axial velocity components, as well as pressure, are not defined at $r = 0$ for such grid. More details about axis treatment are discussed by Akselvoll & Moin (1996) and Verzicco & Orlandi (1996), while applications of our cylindrical coordinate solver can be found in Smith *et al.* (2010), Posa *et al.* (2011), Beratlis, Squires & Balaras (2012), Posa & Balaras (2014), Balaras, Schroeder & Posa (2015) and Posa, Lippolis & Balaras (2015). All spatial derivatives are approximated with second-order central differences. For the advancement in time a semi-implicit, exact projection method is utilized (Van Kan 1986). To eliminate constraints on the time step near the axis, the convective and viscous terms for all azimuthal derivatives are advanced using an implicit Crank–Nicolson scheme, while all other terms are advanced explicitly by a third-order Runge–Kutta scheme. For the solution of the Poisson equation, associated with the projection method, a fast Fourier transform (FFT) decomposition along the azimuthal direction is applied and then on each meridian plane of the cylindrical grid the resulting penta-diagonal system is solved using a generalized cyclic reduction method (Swarztrauber 1974). To enforce boundary conditions on a solid body, which does not coincide with the grid, the direct-forcing immersed boundary method by Balaras (2004) is utilized. Details on the solver, together with an extensive validation for a variety of laminar and turbulent flow problems, can be found in Balaras (2004), Yang & Balaras (2006) and Vanella, Posa & Balaras (2014).

The body we considered is shown in figure 1 and is an idealized submarine geometry, outlined in Groves *et al.* (1989). The same configuration was used in the experiments by Jiménez *et al.* (2010*b*) at yaw angle equal to zero. The main difference with the experimental set-up is the geometry of the sail: in the wind tunnel experiments the body was held in place by a support whose cross-section corresponded to that of the sail. Thus, the support mimicked a semi-infinite sail. In the numerical model the sail is represented exactly as specified in Groves *et al.* (1989). The Reynolds number in the experiments, based on the free-stream velocity, U_∞, and the length of the body, L, was equal to $Re_L = 1.2 \times 10^6$.

In the experiments a trip wire was utilized to get a turbulent boundary layer on the surface of the model. The trip wire was located on the bow of the DSub model, $0.25D$

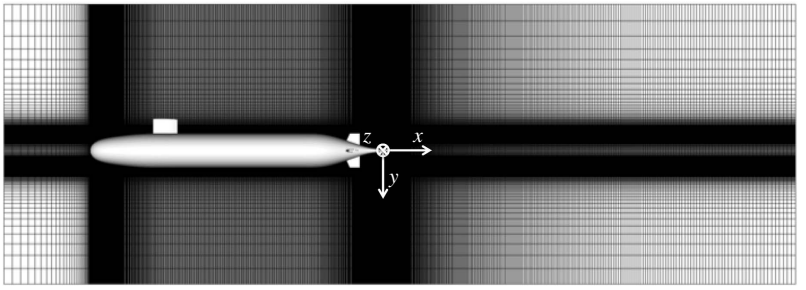

FIGURE 2. Meridian slice of the cylindrical computational grid. For clarity, only one of every four points is plotted along both the radial and the axial directions.

from its nose, where D is the diameter of the cylindrical mid-body. In the simulations the boundary layer is tripped at the same position as in the experiments. The trip wire in the computations was represented by a forcing term distributed locally over a few grid cells around the bow. This treatment lifted the boundary layer, causing locally its separation and then transition after reattachment. The inflow, outflow and lateral boundaries of the computational domain have been placed at $2.6D$ upstream of the nose, $12.2D$ downstream of the tail and at $4.3D$ from the axis, respectively. Note that the DSub length is $L = 8.6D$. At the inflow boundary a uniform free-stream velocity is imposed, while at the outflow boundary a convective boundary condition is used (Orlanski 1976). A slip-wall boundary condition is adopted at the free stream. We also verified on coarser grids that moving further away the inflow section did not affect the solution. The extent of the computational domain downstream of the stern was simply set by how far we could maintain the proper grid resolution with the available computational resources.

The computational grid is composed of $690 \times 1002 \times 4002$ (2.8 billion) nodes along the radial, azimuthal and axial directions. A simplified representation of a meridian slice of the computational grid is provided in figure 2, where for clarity only one of every four points is plotted. It is refined in the radial direction near the cylindrical surface of the hull, to solve accurately the strong gradients inside its boundary layer. Over the cylindrical mid-body, where the turbulent boundary layer is roughly in equilibrium, this resolution places an average number of 8 nodes within the first 12 viscous units of the turbulent boundary layer. In the same region the computational grid is coarser along the axial and azimuthal directions: $\Delta x^+ = 30$ and $(r\Delta\vartheta)^+ = 20$, where r is the radial coordinate and $\Delta\vartheta$ the azimuthal step of the computational grid. The time step in wall-units was $\Delta t^+ = 0.2$. These values are adequate to capture the near-wall dynamics of turbulent boundary layers. Away from the surface of the mid-body the radial resolution was decreased. It is also worth noting that the near-wall resolution requirements decrease over the stern, since the boundary layer grows substantially and the quasi-streamwise vortices move away from the surface. Immediately upstream of the stern appendages, for example, the number of nodes inside the boundary layer along the direction normal to the wall is 220, while in the region between the fins is 260. We placed about 120 nodes along the chord and 28 along the thickness of the fins. The boundary layer over their surface is turbulent, since they are within the thick boundary layer developing along the stern, triggering transition. The average distance of the first node away from the wall for the fin boundary layers is about 2.5 wall-units. The boundary layer over the sail on

the other hand is laminar. We utilized there about 156 nodes along the chord and 30 along the thickness. The axial resolution has been increased in the areas where the grid lines are not aligned with the geometry (the bow and the stern), to improve the isotropy of the computational cells. The stern in particular is one of the most critical regions in this flow problem, because of the presence of the fins and the adverse pressure gradient.

The axial stretching of the grid downstream of the DSub is smooth, to properly resolve its wake. At 6 diameters from the tail, at the radial location of the peak of turbulent stresses ($r/D \approx 0.2$), the grid size is equivalent to about $3 \times 10^{-3}D$, $1 \times 10^{-3}D$ and $1 \times 10^{-2}D$ along the radial, azimuthal and streamwise directions, respectively. With this resolution we verified values of eddy viscosity lower than those of molecular viscosity in the wake region. Note that the design of the final grid was based on the friction velocity evaluated by a coarse direct numerical simulation (DNS) on a coarser grid, composed of 1.75 billion nodes. As discussed above, the final grid was generated by stretching along the radial direction to have about eight nodes between the peak of turbulent kinetic energy in the buffer layer and the surface of the cylindrical mid-body. The comparisons between the two coarse DNS computations in the intermediate wake of the SUBOFF confirmed that the low-order moments were converged on the final grid adopted in the present study.

The flow around the DSub geometry was initially developed at a lower $Re_L = 2 \times 10^5$ and without any perturbation to the boundary layer (no trip wire). Then the Reynolds number was switched to its experimental value $Re_L = 1.2 \times 10^6$ and the boundary layer was tripped on the surface of the bow. After development of statistically steady conditions in the wake the numerical results were sampled over one flow-through time. Note that the sensitivity of the statistics to the size of the sampling period was verified on an earlier coarse DNS, carried out using the same computational grid. The comparison between sampling periods of 1 and 1.5 flow-through times showed convergence for both first- and second-order moments, within 1 % and 5 %, respectively.

3. Results

3.1. *Overview of the flow*

In figure 3 instantaneous fields of the vorticity magnitude are shown on the meridian planes a, b and $c2$ defined in figure 4(a). The effectiveness of the numerical trip wire is evident, as the boundary layer becomes turbulent immediately downstream of the tripping location. In computations where the disturbance was switched off (not shown here), the boundary layer transitioned only directly downstream of the sail, which caused early separation at the stern and a consequent displacement of the wake. When the trip wire is used no separation occurs along the stern. Figure 3(a) highlights that the main areas of turbulent activity, in addition to the boundary layer, are the wake of the fins and the sail. The wake of the sail affects the turbulent boundary layer on the upper side of the hull. The turbulent structures generated in the wake of the sail, however, are not the main feature of the flow in the near and the intermediate wake of the overall body, which is dominated by the structures generated at the trailing edge of the fins and in the thick boundary layer developing along the stern.

In the horizontal plane shown in figure 3(b) the general flow properties are similar. On the plane $c2$ shown in figure 3(c) it is evident that the influence of all appendages (sail and fins) is much weaker than in the previous planes. The vorticity field displays two maxima away from the axis. As we will discuss below, these are due to the

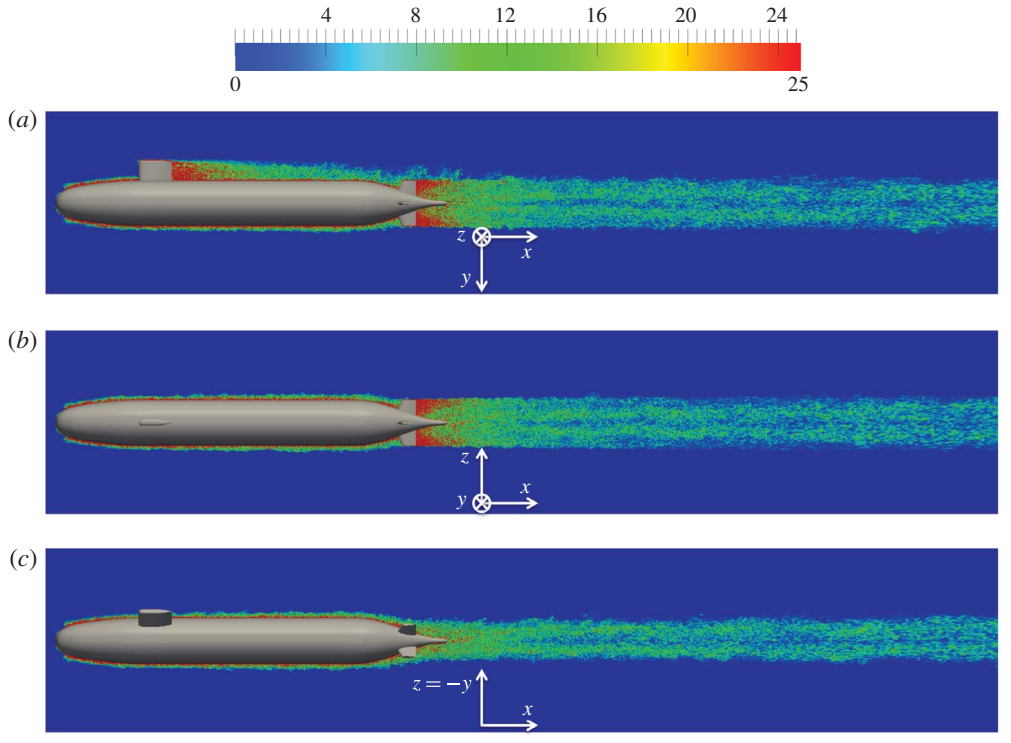

FIGURE 3. (Colour online) Instantaneous fields of the non-dimensional vorticity $\omega D/U_\infty$, where U_∞ represents the free-stream velocity: plane a (a), plane b (b) and plane $c2$ (c). For the orientation of the meridian planes refer to figure 4.

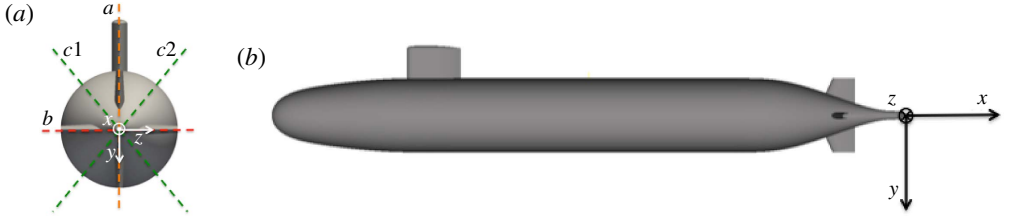

FIGURE 4. (Colour online) (a) Projection of the meridian planes a, b, $c1$ and $c2$ on the cross-stream plane yz. (b) Lateral view of the DSub model representing the position of the reference frame.

boundary layer developing along the stern: the adverse pressure gradient at the rear of the DSub causes a displacement of the peaks of turbulent activity away from the surface of the stern and thus away from the axis of the wake. A more detailed view of the flow along the stern is shown in figure 5, where instantaneous vorticity on cross-sections is shown. It is clear that the flow upstream of the appendages on the stern is mainly affected by the turbulent structures in the boundary layer developing along the stern and less by the sail wake. On the section A–A the highest values of instantaneous vorticity are associated with the flow from the tip of the fins, where the strongest unsteady activity is observed. Looking at the downstream evolution along

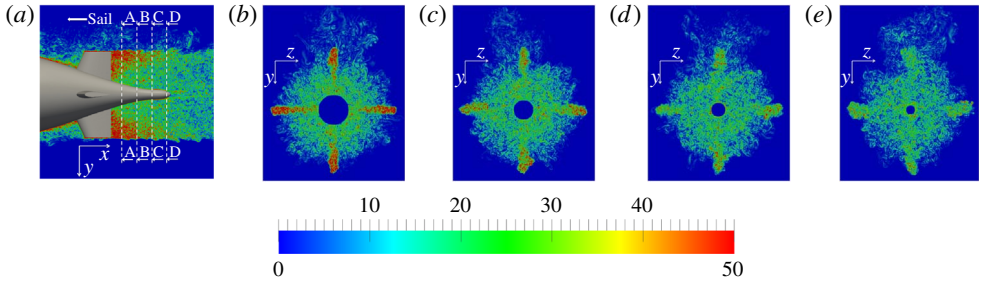

FIGURE 5. (Colour online) Instantaneous magnitude of the non-dimensional vorticity $\omega D/U_\infty$ in the near wake of the fins. In (*a*) a detail of the field in figure 3(*a*) is represented, showing the location of the cross-sections A–A (*b*), B–B (*c*), C–C (*d*) and D–D (*e*).

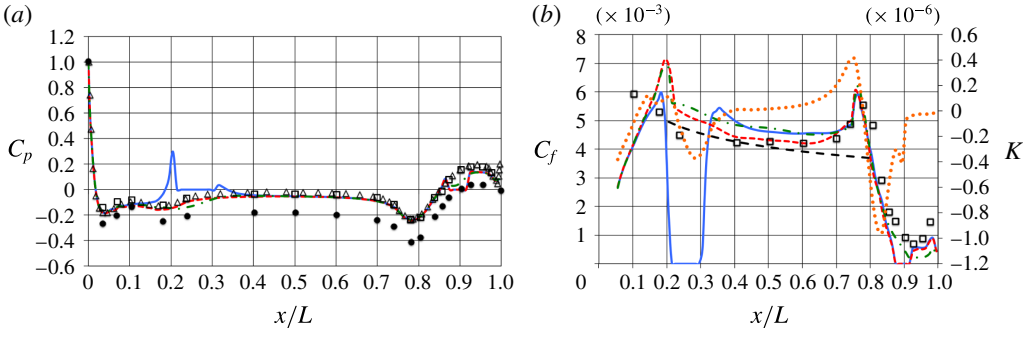

FIGURE 6. (Colour online) (*a*) Time-averaged pressure coefficient; (*b*) time-averaged skin-friction coefficient and acceleration parameter K at different locations along the DSub surface. Present results: —— plane *a* on the side of the negative y axis (location 1); – – – plane *a* on the side of the positive y axis (location 2); — · — average between planes *c*1 and *c*2 on the side of the negative y axis (location 3). Experimental results: □ Huang *et al.* (1994) at $Re_L = 12 \times 10^6$; • Jiménez *et al.* (2010*a*) at $Re_L = 1.1 \times 10^6$. △ RANS computation by Gorski, Coleman & Haussling (1990) on the unappended DSub at $Re_L = 12 \times 10^6$. ——— C_f slope for a zero-pressure-gradient turbulent boundary layer on a flat plate (Schlichting 1968). In (*b*) the acceleration parameter K is also reported as •. The C_f distribution by Huang *et al.* (1994) was rescaled, based on the Reynolds numbers ratio.

the stern, one can see that the vorticity due to the flow from the tip of the fins fades out more quickly than that originated from the boundary layer. This is also one of the main features of the wake and will be discussed in detail in the next section. We should also note that the instantaneous vorticity magnitude above is simply used to provide a qualitative overview of the main flow features. Given the dependence of the vorticity fields on the SGS modelling (see, for example, Galperin 1993) we do not report vorticity statistics in the present work.

3.2. *Statistics along the surface of the body*

In this section the evolution of the boundary layer along the hull is discussed. As the symmetry around the axis is lost due to the presence of the appendages, the evolution of the boundary layers is different on different azimuthal planes. In figure 6

the pressure, C_p, and skin-friction, C_f, coefficients:

$$C_p = \frac{p - p_\infty}{\frac{1}{2}\rho U_\infty^2}, \quad C_f = \frac{\tau_w}{\frac{1}{2}\rho U_\infty^2}, \tag{3.1a,b}$$

are shown at different planes. Note that p_∞ is the free-stream pressure at the inflow plane, ρ the density of the fluid, and τ_w the wall stress. The variation along the plane a, for both negative (location 1) and positive (location 2) y coordinates, and the average along planes $c1$ and $c2$ (location 3) are shown (see figure 4 for the definition of the different planes). The experimental results by Huang *et al.* (1994) and Jiménez *et al.* (2010*a*) as well as the computations by Gorski *et al.* (1990) are included. In both experiments the geometry has no stern appendages, while the Reynolds numbers are 12×10^6 and 1.1×10^6, respectively. The C_p distribution by Gorski *et al.* (1990) comes from a RANS simulation of the flow around the unappended DSub model at Reynolds number equal to 12×10^6. A body-fitted grid was utilized in that case. The reference measurements have been carried out in areas away from the direct influence of the support and are, therefore, comparable to the numerical results at location 2, where the effect of the sail is minimal. The present results are in good agreement with both the measurements by Huang *et al.* (1994) and the computations by Gorski *et al.* (1990). It is interesting to note that the RANS computations by Gorski *et al.* (1990) reproduce accurately the distribution of the pressure coefficient, indicating that in the absence of separation phenomena and secondary flows RANS captures the displacement caused by the boundary layers fairly well. The same computations, however, also point to the limitations of RANS to accurately predict important quantities, such as the skin-friction coefficient, C_f: their results indicate that doubling the grid resolution along the radial and axial directions resulted in an increase of about 50 % for C_f. The same trends have been observed in the study by Alin *et al.* (2010), who simulated both unappended and appended DSub at $Re_L = 12 \times 10^6$ using RANS, DES and wall-modelled LES. They compared their C_p and C_f distributions to the experiments by Huang *et al.* (1994), and while C_p was predicted accurately by all models, C_f was underestimated in all cases. The RANS results had the most significant deviations from the experiments, especially in the stern region, where strong adverse pressure gradients are generated by the hull geometry. Similar results were reported by Bhushan *et al.* (2013), who simulated the appended DSub at $Re_L = 12 \times 10^6$ by URANS, DES and hybrid RANS/implicit LES: the C_p distribution was predicted equally well by all methods, while C_f was best captured by the hybrid RANS/LES methodology.

In our computations the overall evolution of C_p agrees with the results by Jiménez *et al.* (2010*a*), although there is an offset. Jiménez *et al.* (2010*a*) suggested that this offset is likely caused by a different value of the reference pressure. They adopted as p_∞ the pressure at $14.75D$ upstream of the model nose, while Huang *et al.* (1994) considered a location above the model at $x/D \approx 7.3$, that is $1.3D$ upstream of its tail; in the present case the reference pressure was taken at the inflow, which is at $2.6D$ from the nose. Our numerical experiments on coarser grids indicate that the location of the inflow plane relative to the nose has a small effect on C_p, suggesting that this may not be the reason for the disagreement, which is likely due to blockage. Jiménez *et al.* (2010*a*) reported a blockage in their closed-loop wind tunnel, due to both SUBOFF body and support, equal to 5.7 %, while in our computational domain it was only 1.4 %. Furthermore, the wake of the support is obviously much wider than that of the actual sail, considered in this numerical study. Note that the measurements by Jiménez *et al.* (2010*a*) shown in figure 6(*a*) are from the side opposite to the support.

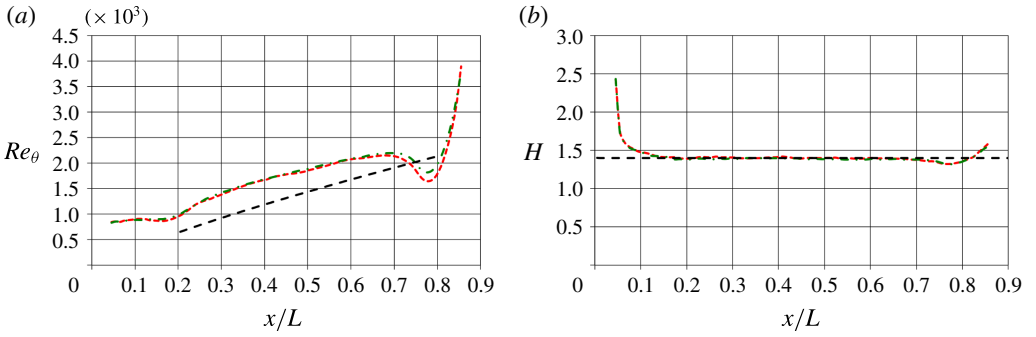

FIGURE 7. (Colour online) Time-averaged (a) momentum thickness Reynolds number, Re_θ, and (b) shape factor, H, along the DSub surface. Present results: −−− plane a on the side of the positive y axis; — · — average between planes $c1$ and $c2$ on the side of the negative y axis. ——— ZPGFPBL (Schlichting 1968).

The evolution of the skin-friction coefficient at the same locations is shown in figure 6(b), together with the acceleration parameter $K = (\nu/U_t^2)(\mathrm{d}U_t/\mathrm{d}s)$ at location 3 (U_t is the local tangential velocity at the edge of the boundary layer and s the coordinate along the local streamline). In this case the slope of C_f for a zero-pressure-gradient turbulent boundary layer along a flat plate (ZPGFPBL) has been added for reference. The evolution of C_f at all positions is very similar, up to the edge between the bow and the mid-body ($x/L \approx 0.2$). Due to the curvature of the body a peak is present there, associated with the acceleration of the flow, as indicated by K. It is likely that the blockage by the sail causes higher values of C_f at the azimuthal location 3 (closer to the sail) than at the location 2, on the opposite side. Also note that at position 1, immediately downstream of the sail, the value of C_f is even larger, compared with the other profiles, due to the junction flows, which bring high momentum fluid towards the root of the sail. Downstream of the sail the rate of change of C_f is very close to that of a ZPGFPBL, especially on the side away from the sail, which is consistent with the nearly zero values of the acceleration parameter in that region. At the beginning of the stern ($x/L \approx 0.75$) the profiles of C_f collapse again, which suggests that the influence of the sail wake becomes negligible, at least on the development of the boundary layer along the stern, where the flow decelerates significantly, as indicated by K. Downstream of the fins the skin friction is higher in their wake than in the planes away due to the junction flows. Both the pressure and the skin-friction coefficients show that near the tail the flow experiences a slight acceleration and then a deceleration due the change of curvature of the stern.

The experiments by Jiménez *et al.* (2010*a*) do not report C_f distributions to compare directly with the present LES. In figure 6(b), however, we included the results by Huang *et al.* (1994) at a much higher Reynolds number ($Re_L = 12 \times 10^6$), rescaling them using the Reynolds numbers ratio. Note that these are measurements on a bare hull configuration. The comparison with the present results is good especially in the area downstream of the sail. Upstream of the sail the predicted C_f is higher than the experiment probably due to the acceleration caused by the sail. The same trend has been reported in the computations by Alin *et al.* (2010).

In figure 7 the evolution of the Reynolds number based on the momentum thickness, $Re_\theta = \theta U_\infty/\nu$, and the shape factor, $H = \delta_1/\theta$, where δ_1 is the displacement thickness and θ the momentum thickness, are plotted downstream of the trip for positions 2

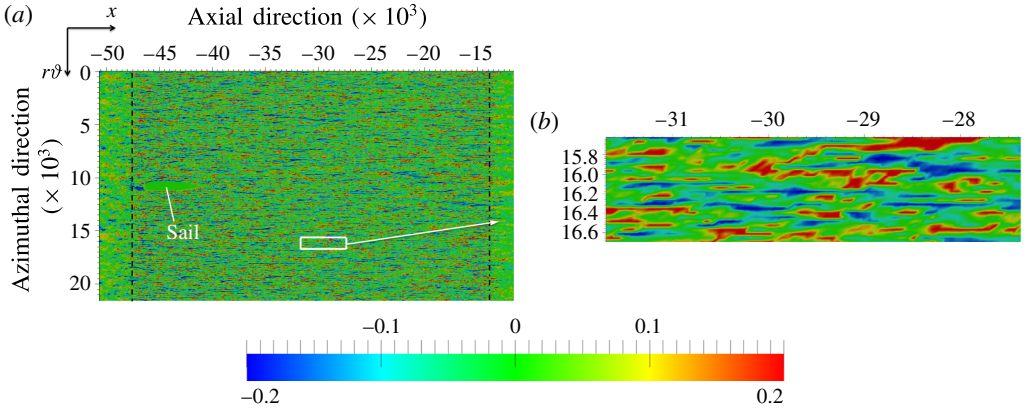

FIGURE 8. (Colour online) Streamwise velocity fluctuations relative to the mean field on an 'unrolled' cylindrical slice of the computational grid at 10 wall-units from the surface of the mid-body. The coordinates along the spanwise and streamwise directions are provided in wall-units. The fluctuations are non-dimensionalized by the free-stream velocity, U_∞. Note that the origin of the streamwise axis is located at the tail of the stern. (*a*) Global view, where −−− and — · — represent the beginning and the end of the cylindrical mid-body; (*b*) detail, shown in (*a*) by a white box, at an azimuthal location 90° away from the sail in the mean streamwise region of the mid-body.

and 3 (position 1 is not shown, since it is strongly affected by the wake of the sail). The corresponding slope for a ZPGFPBL has been added for comparison. Along the mid-body the slope of Re_θ, as well as H, compares fairly well with that of a ZPGFPBL, indicating that in this region the boundary layer is almost in equilibrium. Outside this region deviations from this behaviour can be observed. Re_θ, for example, shows an increased slope just downstream of the edge between the bow and the mid-body ($x/L \approx 0.2$), due to a mild adverse pressure gradient (see figure 6*a*). The slope decreases along the cylindrical mid-body, because of the gradual reduction of the pressure gradient. This trend becomes more obvious between $x/L = 0.7$ and $x/L = 0.75$, due to the local acceleration of the flow (the thickness of the boundary layer is decreasing). Along the stern the boundary layer grows significantly. The agreement between the numerical profiles is very close up to the appendages on the stern ($x/L = 0.85$), which shows that the influence of the sail wake is limited.

Next we will take a closer look at the boundary layer in the mid-body area. Figure 8 shows a snapshot of the instantaneous streamwise velocity fluctuations on an unrolled cylindrical slice of the computational grid 10 wall-units away from the surface (the average u_τ in the range $0.3 < x/L < 0.6$ is used for all inner scaling). The coordinates along the azimuthal and axial directions are provided in wall-units. The presence of the typical streaks, associated with the quasi-streamwise vortices inside the boundary layer, is visible. It is also interesting that the sail does not affect significantly the streaks in its wake. In the detailed view (figure 8*b*) the actual dimension of the streaks is shown and is in agreement with the values reported in the literature: their streamwise extent is in the order of 1000 wall-units and their spacing along the cross-stream direction is equivalent to few hundreds wall-units.

In figure 9 velocity statistics inside the boundary layer are shown in inner coordinates for both the azimuthal location aligned with the sail and the opposite one. Both mean velocity profiles have a logarithmic region with a slope that is in

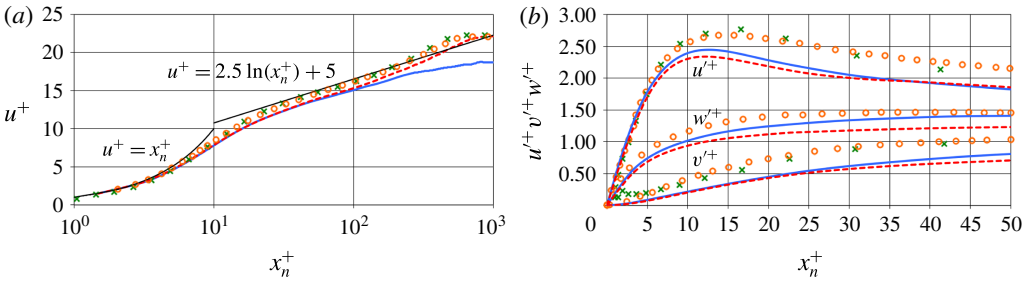

FIGURE 9. (Colour online) Statistics in wall-units in the turbulent boundary layer at the mean streamwise position of the DSub model: −−− along the positive y axis (side away from the sail); —— along the negative y axis (side downstream of the sail); ○ DNS on a ZPGFPBL by Spalart (1988) at $Re_\theta = 1410$; × measurements by DeGraaff & Eaton (2000) at $Re_\theta = 1430$. (*a*) Time-averaged streamwise velocity u; (*b*) root mean squares u', w' and v' of the streamwise, spanwise and normal velocity components. Here x_n^+ is the local coordinate in wall-units along the direction normal to the wall.

agreement with that of the universal law for a ZPGFPBL; however, their intercept is smaller, maybe due to the presence of the upstream sail, affecting the distribution of the skin-friction coefficient and friction velocity along the surface of the DSub, which are higher than those for a ZPGFPBL. At the edge of the boundary layer ($x_n^+ \approx 1000$) a deviation between the profiles on the opposite sides is observed: on the side away from the sail the wake of the turbulent boundary layer is clearly distinguishable, while its formation is prevented by the wake of the sail on the other side. The velocity fluctuations (see figure 9*b*) are slightly underestimated in comparison with the values in the literature (Spalart 1988; DeGraaff & Eaton 2000), which is probably due to the higher values of friction velocity. Grid resolution could also affect this behaviour, but due to the large computational cost of the present simulation further grid refinement was prohibitively expensive. However, based on the evolution of the acceleration parameter reported in figure 6(*b*), a deviation of the statistics in the boundary layer from those of a ZPGFPBL can be expected: the present case displays a complex pattern of accelerations/decelerations, also dependent on the particular azimuthal position over the SUBOFF surface. At the same time the grid resolution over the cylindrical mid-body satisfies the requirements reported in the literature for wall-resolved LES (Georgiadis, Rizzetta & Fureby 2010).

3.3. *Comparison with the experiments*

In figure 10 the present results in the intermediate wake (6D from the tail) are compared with the hot wire measurements by Jiménez *et al.* (2010*b*) at $z/D = 0$, corresponding to the plane through the sail. In figure 10(*a*) the comparison is provided in self-similar coordinates, which are the maximum velocity deficit, u_0, the difference between the free-stream velocity and the minimum velocity in the wake, and the half-wake width, l_0, the distance between the centre of the wake and the location where the momentum deficit is equal to $u_0/2$. The similarity law for the mean streamwise velocity, proposed by Jiménez *et al.* (2010*b*), is also included, where $\eta = y/l_0$:

$$f(\eta) = \exp(-0.525\eta^2 - 0.1375\eta^4 - 0.03\eta^6 - 0.002225\eta^8). \tag{3.2}$$

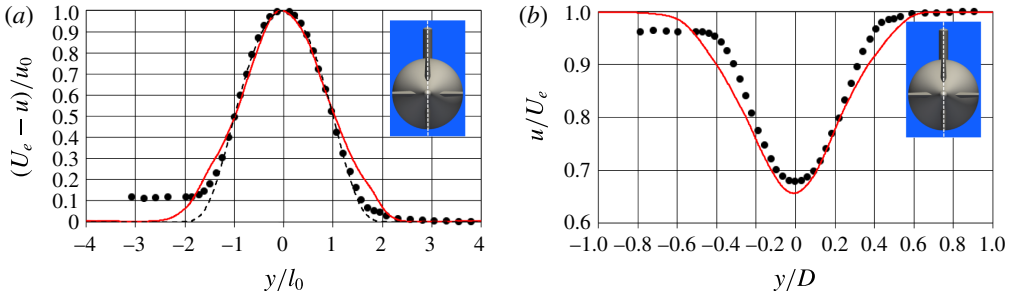

FIGURE 10. (Colour online) (*a*) Time-averaged streamwise velocity defects in similarity coordinates (the profiles are scaled by the maximum velocity defect, u_0, and the half-wake width, l_0; U_e is the velocity at the edge of the wake). (*b*) Time-averaged streamwise velocity profiles, scaled by U_e and D. Position at $x/D = 6$ and $z/D = 0$. – – –, (3.2); •, experiments by Jiménez *et al.* (2010*b*); ——, LES.

In figure 10(*a*) for $-1 < y/l_0 < 1$ the agreement between all profiles is very close. For $1 < |y/l_0| < 2$ on both sides the velocity defect in the numerical results is a little larger than in the experiments, probably due to the fact that this region is affected by wake of the fins. For $|y/l_0| > 2$ the agreement with the experiments is again satisfactory on the side opposite to the sail. On the other side the numerical profile meets the theoretical curve much better than the experiments. This can be explained considering the larger velocity deficit produced in the wind tunnel by the wake of the support. In figure 10(*b*) the profiles of streamwise velocity are scaled by U_e (velocity at the edge of the wake) and D. The agreement with the experiment is good and the differences between measurements and computations can be justified: for negative y coordinates the experimental profile does not recover the free-stream velocity, being affected by the large wake of the support. The blockage it generates is the likely reason of the higher velocities seen in the experimental profile for $y/D > -0.5$. We verified that this effect is even more obvious in the offset planes, therefore at those locations we assumed more appropriate to compare between computations and experiments in self-similar coordinates: in figure 11 two offset planes are considered, for $z/D = 0.125$ and $z/D = 0.250$, respectively. The agreement between simulation and experiments is again very good, and the largest discrepancies can be seen at $y/l_0 \approx -2$, due to the strong influence of the support in the experiments.

A more global picture of the averaged velocity field is shown in figure 12, where the time-averaged streamwise velocity in the same planes considered in figure 3 is shown. Note that in figure 12(*c*) the average between the planes *c*1 and *c*2 (see figure 4) is plotted. The comparison among the three different fields further highlights the influence of the appendages on the stern to the mean flow. In the planes *a* and *b*, especially in the vicinity of the DSub, an additional lack of momentum at the edge of the wake can be observed, relative to the field on the *c* planes, due to the flow from the tip of the fins. As discussed above, this result has been verified also experimentally by Jiménez *et al.* (2010*b*), who found that the main deviation from the wake of the unappended geometry is downstream of the tips of the stern appendages. Instead, figure 12(*c*) shows that in the planes away from the fins the near wake has a smaller diameter than that of the cylindrical mid-body, since the boundary layer on the stern stays attached, following the curvature of its surface. Further downstream the width of the wake on all three planes tends to converge, due to diffusion along

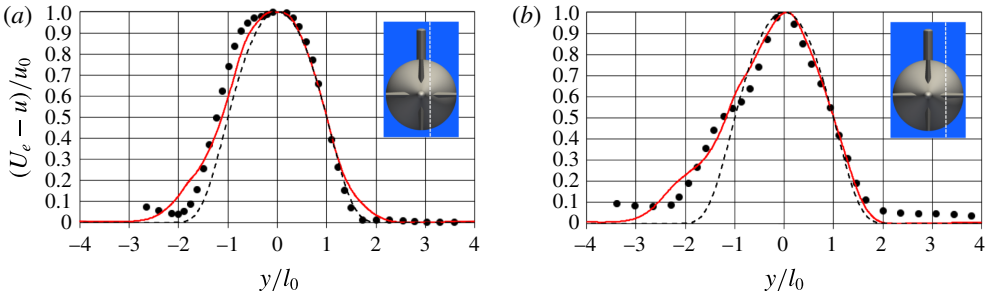

FIGURE 11. (Colour online) Time-averaged streamwise velocity defects in similarity coordinates. Position at $x/D = 6$ and (*a*) $z/D = 0.125$, (*b*) $z/D = 0.250$. – – –, (3.2); •, experiments by Jiménez *et al.* (2010*b*); ——, LES.

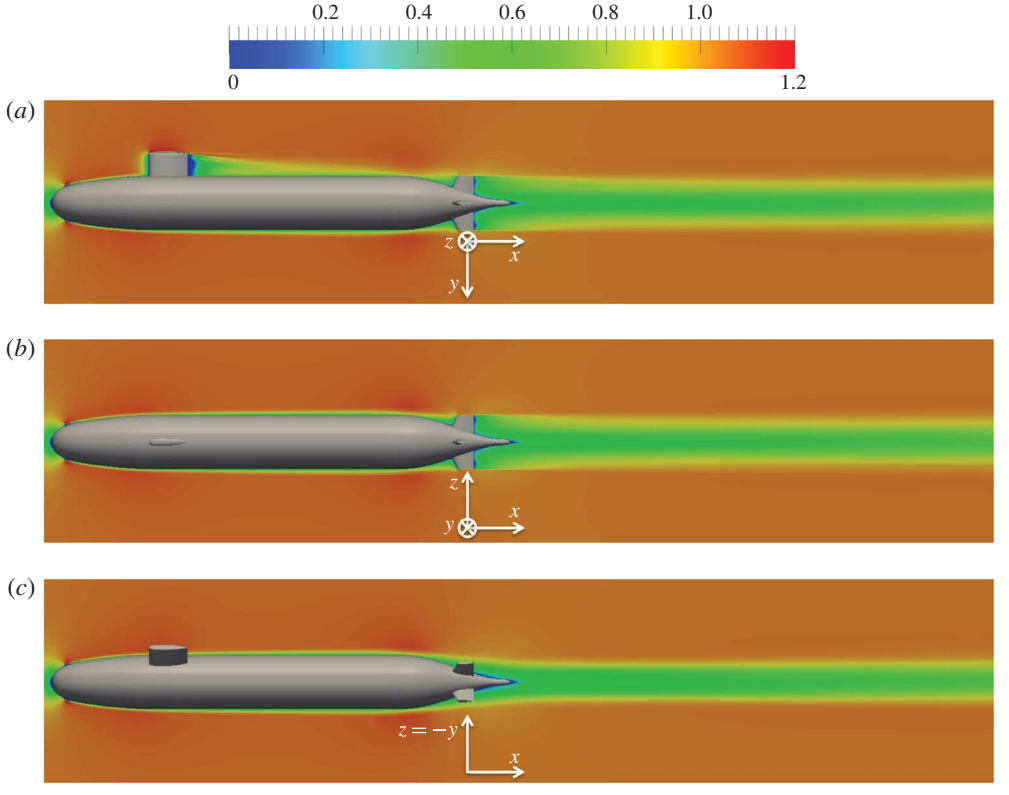

FIGURE 12. (Colour online) Time-averaged fields of the non-dimensional streamwise velocity u/U_∞: plane *a* (*a*), plane *b* (*b*) and average between planes *c*1 and *c*2 (*c*). For the position of the planes see figure 4(*a*).

the azimuthal direction. It is also shown in figure 12(*a*) that on the symmetry plane the overall wake is primarily affected by the momentum deficit caused by the fins and marginally by that associated with the sail, whose influence is mainly limited to the length of the cylindrical mid-body. It is also clear that the flow at the convex border between the cylindrical mid-body and the stern experiences an acceleration,

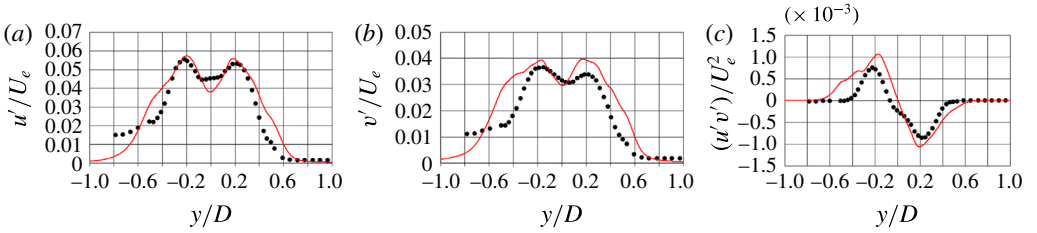

FIGURE 13. (Colour online) R.m.s. of the velocity components along x (a) and y (b), and the shear stress in the xy plane (c). Profiles at $6D$ from the tail of the stern at $z/D = 0$ (plane through the sail). •, experiments by Jiménez *et al.* (2010*b*); ——, LES.

with a consequent local decrease of the boundary layer thickness. This occurs also at the edge between the bow and the mid-body, although it is less evident in figure 12. The same behaviour has been observed in the experiments by Huang *et al.* (1994) and Jiménez *et al.* (2010*a*) and in the RANS simulations by Gorski *et al.* (1990).

In figure 13 the profiles for the root mean square (r.m.s.) of the streamwise and radial velocity components and the shear stress in the xy plane are shown at $x/D = 6$ and $z/D = 0$, normalized by the velocity at the edge of the wake and the maximum hull diameter. These results are not plotted in similarity coordinates, because the Reynolds stresses are not self-similar at this distance from the stern. More details on this issue can be found in Jiménez *et al.* (2010*a*,*b*). The agreement between the experiments and the simulation is very good. The peaks at $y/D = \pm 0.2$ are accurately captured by the computation. Some deviations can be seen around $y/D = \pm 0.5$ and on the axis. On the side downstream of the sail at the edge of the wake the deviation of the experiments from the numerical results for $y/D < -0.5$ is due to the support: the effect of the sail wake in the simulation is much more localized than in the wind tunnel experiments and the r.m.s. go to 0, which implies a more symmetric profile. The radial velocity fluctuations (figure 13*b*) are slightly over-predicted in comparison with the experiment near the axis ($-0.2 < y/D < 0.2$). The wake of the appendages on the stern also causes higher fluctuations ($0.4 < |y/D| < 0.6$). The bimodal distribution and the location of the maxima away from the axis of the wake are captured accurately.

The comparison on the shear stress is shown in figure 13(c); it is consistent with the ones for the r.m.s. of u and v. The experiments and the computation agree on the presence of 2 maxima away from the axis and on their location, although the numerical values are slightly higher. This behaviour is in line with the observations in the experiments by Jiménez *et al.* (2010*a*,*b*), who found that for the unappended geometry the semi-infinite sail had a destructive influence on the shear stress $u'v'$, while the interaction of the wake of the support with that of the fins caused increased shear stresses for negative y coordinates downstream of the appended DSub.

3.4. *Bimodal behaviour of the wake and effect of the fins*

The results in the intermediate wake by Jiménez *et al.* (2010*a*,*b*), as well as the present simulation, show a bimodal behaviour for the normal stresses. Jiménez *et al.* (2010*a*,*b*) attributed it to the thick boundary layer developing along the stern of the DSub model. This is consistent with observations in earlier experiments by Patel, Nakayama & Damian (1974) and Merz, Yi & Przirembel (1986). In figure 14 the averaged turbulent kinetic energy, k, is shown at three different meridian planes up

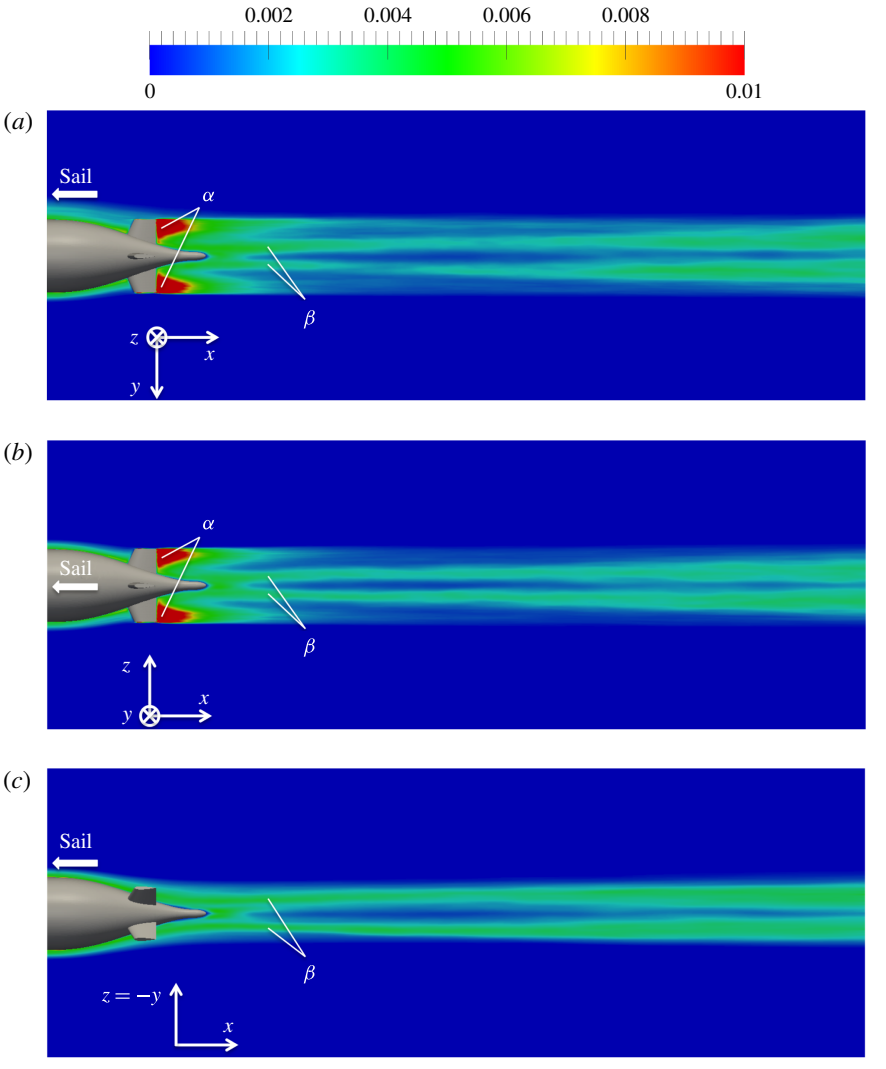

FIGURE 14. (Colour online) Fields of k/U_∞^2 in the wake up to $9D$ from the stern tail: (*a*) plane *a*; (*b*) plane *b*; (*c*) average between planes *c*1 and *c*2. See figure 4 for the location of the planes. The position of the upstream sail is indicated by a white arrow. Here α and β are the regions of high turbulent kinetic energy associated respectively with the wake of the fins and the thick boundary layer shed from the stern surface.

to nine hull diameters from the tail of the body. In the section through the sail (see figure 14*a*) the highest values of k are reached in the wake of the fins at their tips (marked α in the figure). This wake, however, fades out quickly and further downstream the local maxima originating from the boundary layers on the stern (marked β in the figure) become rapidly the most distinguishable feature of the wake just few diameters from the tail. The wake spreads radially, but the minimum of k at the axis is still visible several diameters from the body. The field in figure 14(*b*), referring to the meridian section orthogonal to the axis of the sail, has similar features, but in this plane the distribution is practically symmetric. At the meridian

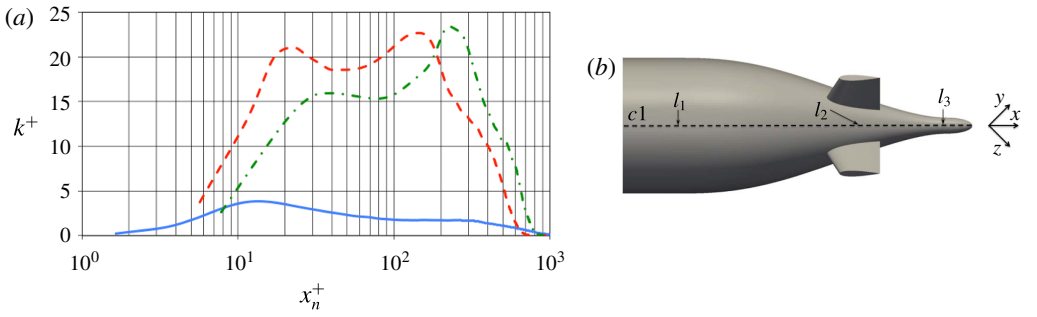

FIGURE 15. (Colour online) Profiles of turbulent kinetic energy in inner coordinates (*a*) on the *c* planes on the side away from the sail along the normal directions l_1 (——), l_2 (— — —) and l_3 (— · —), whose intersections with the surface of the submarine are indicated in (*b*) by arrows. Averages between the distributions on the $c1$ and $c2$ planes. In (*b*) the projection of the $c1$ plane on the DSub is also shown by a dashed line.

plane between the fins (figure 14*c*) the distribution of k is slightly asymmetric in the near wake, due to the stronger turbulence on the side of the sail. Overall it is clear that in the near wake the peaks of k in the planes *a* and *b* through the appendages (see figure 4*a* for their definition) are closer to the axis, compared with those in the *c* planes, which indicates an influence by the junction flows. Indeed Jiménez *et al.* (2010*b*) compared the wakes without and with appendages on the stern and verified that the dual peak behaviour of the r.m.s. of the velocity components u and v is enhanced by the presence of fins.

To better understand the origin of this behaviour figure 15(*a*) shows the evolution of the turbulent kinetic energy profiles at the stern along the l_1, l_2 and l_3 directions normal to the body (see figure 15*b*). As expected, at the first location, l_1, the turbulent kinetic energy peaks at about $x_n^+ = 12$, since the effects of pressure gradients on the turbulent boundary layers are still mild. At l_2, between the fins, the evolution is significantly modified and a second peak appears away from the wall at $x_n^+ \approx 100$. The same trend can be seen at l_3, where the maximum away from the wall is significantly stronger than the near one. These phenomena are consistent with the results reported in the literature for boundary layers under strong adverse pressure gradients, which were found to have the same effect on turbulent fluctuations: a new peak is generated away from the wall, while the inner maximum fades out, as shown in several studies (Spalart & Watmuff 1993; Skåre & Krogstad 1994; Song & Eaton 2004; Aubertine & Eaton 2005; Lee & Sung 2008; Monty, Harun & Marusic 2011). Therefore, the bimodal distribution in the DSub wake is associated with the generation of an outer peak of the fluctuations inside the turbulent boundary layer. It is also worth noting that the modified distribution of the turbulent kinetic energy under the adverse pressure gradient is actually due to a significant decrease of the near-wall turbulence in the buffer layer, while that in the outer layer is almost unchanged, which is again in agreement with the above literature.

We observed that the decrease of the velocity fluctuations in the inner layer and the displacement of the turbulence peak in the outer layer are associated with the behaviour of the quasi-streamwise vortices along the stern. Under the effect of the adverse pressure gradient at the rear of the body their density decreases and they experience a displacement away from the surface, towards the outer layer. This is evident in figure 16(*a*), where the second invariant of the velocity gradient tensor

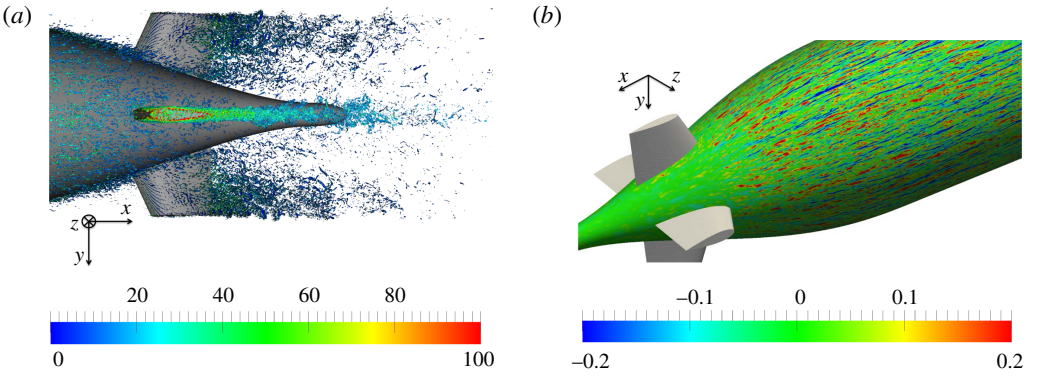

FIGURE 16. (Colour online) (*a*) Visualization of the coherent structures at the stern of the submarine using the Q-criterion (Hunt, Wray & Moin 1988), with representation of the vorticity magnitude, scaled by the free-stream velocity, U_∞, and the hull diameter, D. (*b*) Streamwise velocity fluctuations, normalized by the free-stream velocity U_∞, at a distance from the wall equivalent to 20 wall-units (referred to the mid-body location).

is used to isolate the coherent vortices in the flow (Hunt *et al.* 1988). At the rear of the body coherent structures are actually coming mainly from the fins, releasing hairpin vortices into the wake. In figure 16(*b*), the streamwise velocity fluctuations are shown on a surface located 20 wall-units (based on the average wall stress at the mid-body) away from the body. The presence of streaks near the wall of the cylindrical mid-body is obvious, but along the stern they are visible only at larger distances from the SUBOFF surface, as we verified by similar visualizations further away from the wall (not reported here).

The effect of the junction flows on the velocity fluctuations is shown in figure 17(*a*), where the evolution of the turbulent kinetic energy is plotted along l_2 at the azimuthal locations indicated in figure 17(*b*). The increase of turbulence near the root of the fins is evident on the e and f planes, which is due to the junction flows. The profiles in outer coordinates verified that the outer maximum is not substantially modified closer to the fins, while the inner one is highly enhanced, on both the e and f planes. However, it will be shown that further downstream this additional turbulence tends to move away from the surface of the body, enhancing the outer peak. Therefore, the LES results partially confirmed the hypothesis formulated by Jiménez *et al.* (2010*b*) about the effect of the stern appendages on the velocity fluctuations. Their comparison between unappended and appended case showed a more obvious bimodal behaviour in the latter. This result was attributed to vorticity production associated with the junction and tip flows from the fins. The present computations actually verified that turbulence coming from the tip of the appendages decays very quickly in the near wake, as evident in figure 14, while the outer peak of turbulence in the stern boundary layer is actually reinforced by the junction vortices. Figure 17(*b*) provides a broader view of the behaviour of k on the r–ϑ plane where l_2 crosses the surface of the stern. Away from the fins the field of turbulent kinetic energy shows an obvious azimuthal region of higher turbulence, which is associated with the outer peak in the thick boundary layer developing along the stern. Near the fins the turbulent kinetic energy is clearly affected and the peak is much closer to the surface of the stern.

At the l_3 location, which is closer to the tail, the values of turbulent kinetic energy in inner coordinates decrease moving towards the appendages (see figure 18*a*). This

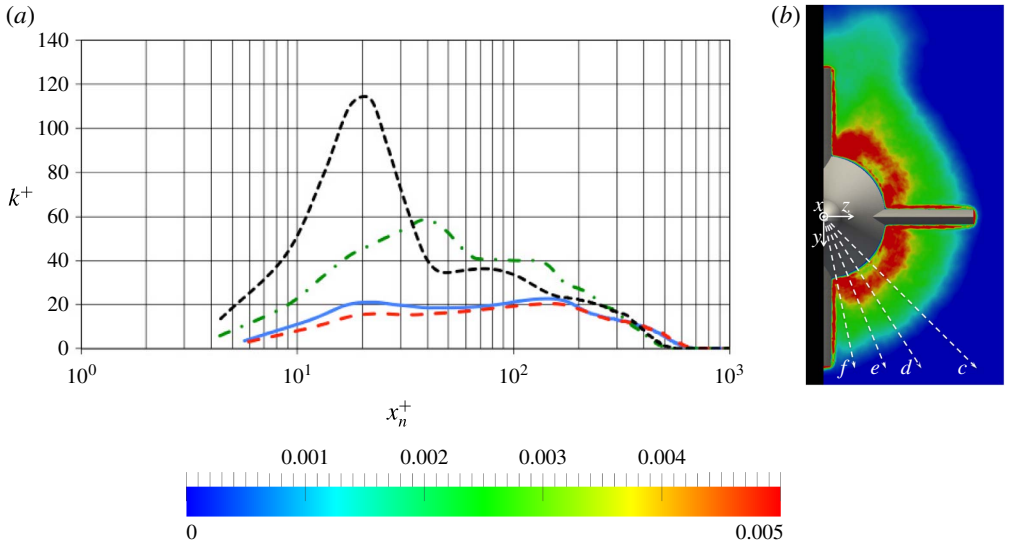

FIGURE 17. (Colour online) (*a*) Profiles of turbulent kinetic energy in inner coordinates on the semi-planes represented in (*b*) along the normal direction at the location l_2 in figure 15 —— *c*, ———— *d*, — · — *e*, – – – *f*; (*b*) field of k/U_∞^2 in the r–ϑ plane at the streamwise location l_2. In both (*a*) and (*b*) averages based on the symmetry relative to the plane of the sail.

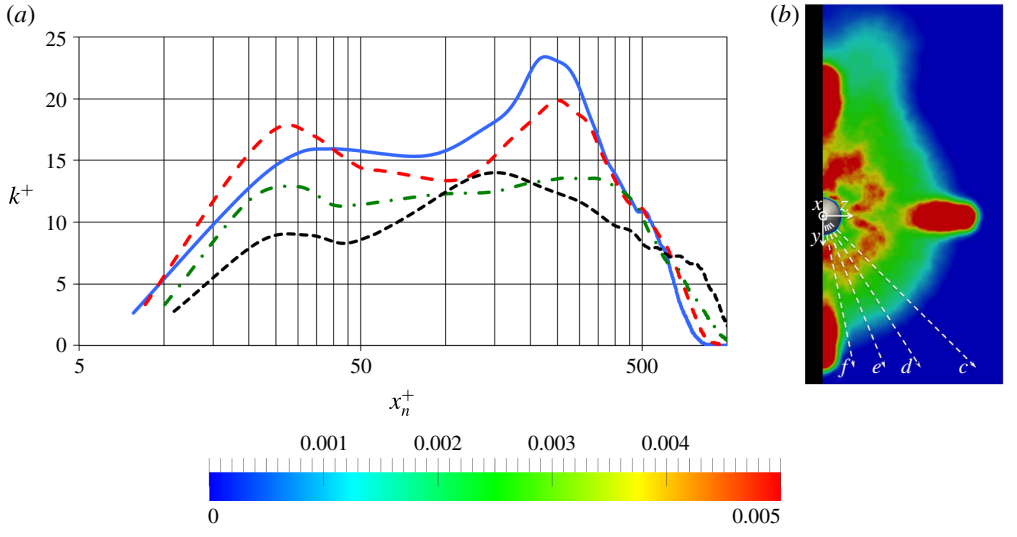

FIGURE 18. (Colour online) (*a*) Profiles of turbulent kinetic energy in inner coordinates on the semi-planes represented in (*b*) along the normal direction at the location l_3 in figure 15 —— *c*, ———— *d*, — · — *e*, – – – *f*; (*b*) field of k/U_∞^2 in the r–ϑ plane at the streamwise location l_3. In both (*a*) and (*b*) averages based on the symmetry relative to the plane of the sail.

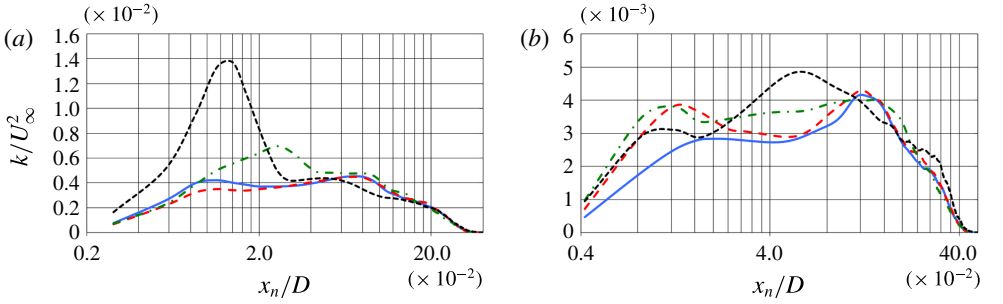

FIGURE 19. (Colour online) Profiles of turbulent kinetic energy in outer coordinates on the semi-planes represented in figure 18(*b*) along the normal directions: —— *c*, ——— *d*, — · — *e*, – – – *f*. Locations l_2 (*a*) and l_3 (*b*) in figure 15. Averages based on the symmetry relative to the plane of the sail.

is due to the increase of the wall stress in the wake of the fins, caused by the junction flows. Figure 18(*b*) shows at the inner radii a decreased level of turbulence in the planes directly downstream of the fins, where turbulence is initially lower in comparison with that downstream of their tip. There is an evident non-uniformity along the azimuthal direction. It has been observed that moving downstream the field of turbulent kinetic energy undergoes a redistribution, becoming more symmetric, which explains the behaviour seen in figure 14 on the *r*–*z* planes. In particular, in figure 14(*a*) one can see at the inner radii a streamwise increase of the peaks of turbulent kinetic energy in the wake, which is due to its redistribution along the azimuthal direction.

To quantify the role of the junction flows on the turbulent kinetic energy near the stern surface, profiles in outer coordinates (at the same locations as in figures 17*a* and 18*a*) are shown in figure 19. At the l_2 location (figure 19*a*) it is verified that the inner peak experiences a substantial increase at the azimuthal positions *e* and *f*. The outer maximum is instead almost unaffected. At the l_3 location (figure 19*b*) it is evident that the effect of the junction flows propagated along the azimuth and towards outer radii. The outer peak is stronger along *f*, showing that also turbulence caused by the junction flows tends to move away from the wall: overall the outer turbulence is higher near the appendages. This result is consistent with the measurements by Jiménez *et al.* (2010*b*), who observed that, even if the bimodal behaviour of the stresses is a main feature also in the wake of the unappended DSub, it is reinforced by the presence of the appendages. Their junction flows feed additional turbulence near the wall and they undergo the same adverse pressure gradient experienced by the boundary layer, causing a displacement away from the wall also for this additional turbulence. As discussed above, the footprint of the junction flows is also visible in figure 14: in the near wake the maxima of turbulent kinetic energy are slightly closer to the axis on the *a* and *b* planes through the fins, than in the *c* planes between them. This behaviour is due to the shorter development along the tail of the submarine of the turbulence associated to the junction flows, compared to that in the stern boundary layer.

In figure 20 the time-averaged tangential velocity profiles in outer coordinates are plotted, showing the overlapping effects of strong streamwise pressure gradients and junction flows generated by the fins. Figure 20(*a*) highlights the variation of the boundary layer shape, by means of the profiles on the *c* planes along the directions l_1, l_2 and l_3 of figure 15(*b*). Along l_3 also the influence of the junction flows is seen

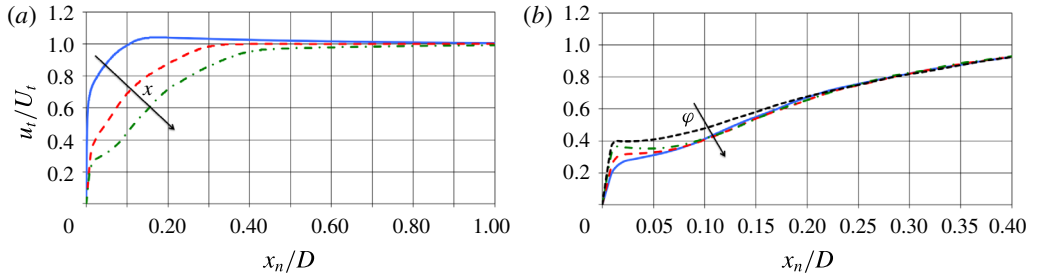

FIGURE 20. (Colour online) Time-averaged profiles of tangential velocity in outer coordinates. (*a*) On the *c* planes along the directions represented in figure 15(*b*): —— l_1, ———— l_2 and — · — l_3; x is the streamwise location of the profiles. (*b*) Along the direction l_3 in figure 15(*b*) on the semi-planes in figure 18(*b*): —— *c*, ———— *d*, — · — *e*, – – – *f*; φ indicates the azimuthal distance from the closest fin.

closer to the wall, where the slope of the velocity profile is locally increased. In fact, although the *c* planes are away from the appendages, at the last streamwise location considered in figure 20(*a*) the radius of the stern is smaller, which increases the azimuthal extent of the junction vortices. In figure 20(*b*) the same velocity profiles along the direction l_3 are plotted, but at different azimuthal distances φ from the fin oriented along the positive y axis, between the *c* and the *f* semi-planes (see figure 18*b*). The junction flows cause higher tangential velocities downstream of the root of the fins. This is consistent with the higher values of skin friction in the wake of the fins and the sail. Note that in figure 20 the symbols u_t and U_t have been adopted to indicate respectively the local and the free-stream tangential velocities, which along the stern differ from the streamwise ones.

3.5. *Evolution towards self-similarity*

For any wake-producing body, and given sufficient distance downstream, the mean flow is expected to be self-similar (Townsend 1956). The wake flow can be characterized through the maximum velocity deficit, u_0, and the half-wake width, l_0. Typically u_0 and l_0 evolve according to a power law. For an axial symmetric wake, for example, $u_0 \propto (x - x_0)^{-2/3}$ and $l_0 \propto (x - x_0)^{1/3}$, where x_0 is the virtual origin of the self-similar wake. In the experimental studies by Jiménez *et al.* (2010*a*,*b*) it was found that the wake of the unappended DSub becomes self-similar for the mean quantities and on the side away from the support in just few diameters downstream from the tail. Figure 21 shows the evolution of u_0 and l_0 along the streamwise direction from the present LES. Note that the values of l_0 in figure 21(*b*) were estimated on the side away from the sail, that is the one along the positive y axis. In the same figure the power law model that best fits the LES data is included together with that proposed by Jiménez *et al.* (2010*b*) for the unappended geometry. The power laws that fit the LES solution are

$$u_0 = 1.57(x + 4.58)^{-2/3}, \quad l_0 = 0.13(x + 4.58)^{1/3}. \tag{3.3a,b}$$

Figure 21(*a*) shows that effectively at three diameters from the tail of the DSub the maximum velocity defect already behaves consistently with the self-similar theory. The numerical values are slightly higher than the experimental fit proposed by Jiménez

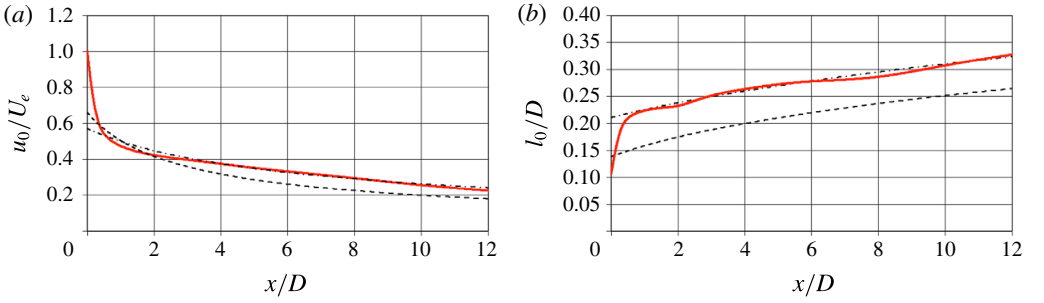

FIGURE 21. (Colour online) Evolution in the intermediate wake of the maximum velocity defect u_0 (*a*) and the half-wake width l_0 (*b*): —— present LES results; — · — present self-similar model (see (3.3)); −−− self-similar model by Jiménez *et al.* (2010*b*) for the wake of the unappended DSub.

et al. (2010*b*) for the unappended geometry. Figure 21(*b*) shows that also l_0 evolves in a self-similar fashion. Compared with the experimental model, the numerical results display significantly higher values, as the presence of the fins increases the width of the wake. The slope of the streamwise evolution however is the same in both cases.

A more detailed comparison with the self-similar solution proposed by Jiménez *et al.* (2010*b*) for the unappended DSub is shown in figure 22. Nine r–ϑ planes are reported in self-similar coordinates, corresponding to a distance of $1D$ through $9D$ from the tail. In each plane the present results are provided on the left. On the right side of each plane the axial symmetric self-similar solution proposed by Jiménez *et al.* (2010*b*) (see (3.2)) has been added. Overall it is clear that the self-similar condition for the mean streamwise velocity in the wake of the appended DSub has not been established yet even at nine diameters from the tail of the stern. In the experiment by Jiménez *et al.* (2010*a*) on the unappended DSub the establishment of a self-similar state on the side away from the sail took only three diameters downstream of the tail. As expected, the appendages on the stern cause a delay in this process. Looking at the isolines in figure 22, it is also interesting to note that the flow coming from the tip of the fins, as well as the wake of the sail, is characterized by an increased momentum deficit, compared with the axial symmetric wake on the right of each plane; on the other hand, the flow from the root of the fins displays a decreased momentum deficit, due to the junction flows, which carry higher momentum fluid downstream of the stern appendages. This different behaviour at the outer and inner radii of the wake can be seen looking at the interface between the isolines of the LES solution and those of the axial symmetric model: the outer isolines on the left side of each panel in figure 22 are displaced towards larger radii and the inner ones towards smaller radii, compared with those associated with (3.2) on the right side.

To look more in detail at the initial development of the wake, where the influence of the appendages is limited to narrow azimuthal regions of the domain, figure 23 shows the radial distribution of the time-averaged velocity deficit in the near wake, plotted in self-similar coordinates. The three different plots refer to the streamwise locations at 1, 2 and 3 diameters from the tail of the body, respectively. In each panel the profiles along the three directions *a*, *b* and *c*, defined in figure 4, are shown. The profiles along *c*1 and *c*2 have been averaged. Note that the radial coordinate is assumed positive on the side away from the sail (positive y axis). Therefore, along the direction *b* positive and negative radial coordinates are equivalent and the profiles

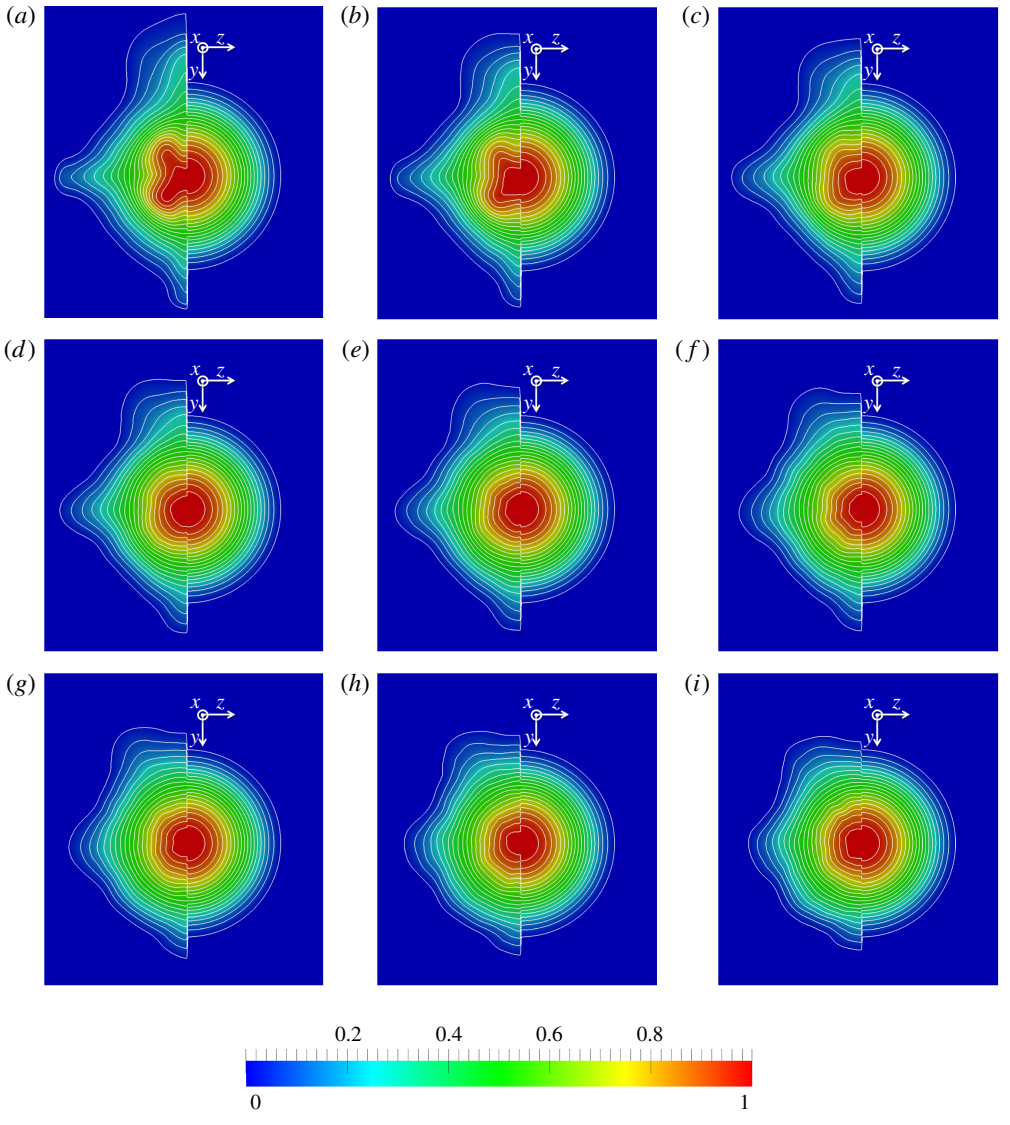

FIGURE 22. (Colour online) Time-averaged fields of the velocity defect in similarity coordinates in the wake of the DSub. The nine downstream locations are at increasing distances from the stern tail, with a step equal to the maximum hull diameter, D. The present numerical solution is shown on the left side, while the self-similar axial symmetric solution proposed by Jiménez *et al.* (2010*b*) is on the right side. Also the isolines are plotted between values of 0.05 and 0.95 using a step equal to 0.05. Note that the representation of the reference frame has been moved from the axis to make the interface between isolines visible.

are expected to be symmetric relative to $r = 0$. The reference self-similar solution is also included in the figure. The development of self-similarity is very fast on the plane away from the direct influence of the appendages (direction c), which is in good agreement with the findings by Jiménez *et al.* (2010*a*) for the unappended DSub.

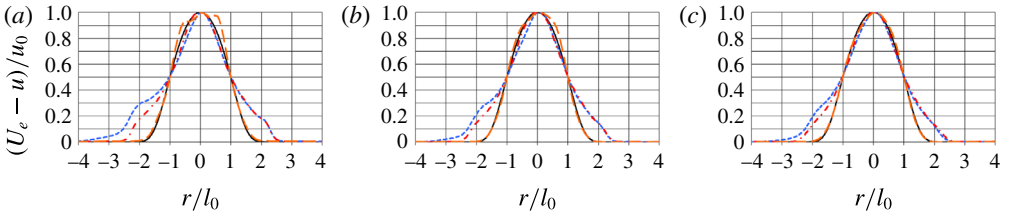

FIGURE 23. (Colour online) Time-averaged velocity defects in self-similar coordinates in the near wake at 1 (*a*), 2 (*b*) and 3 (*c*) diameters downstream of the stern tail. —— (3.2); – – – direction *a*; — · — direction *b*; ———— average between directions *c*1 and *c*2. Note that positive radial coordinates refer to the side away from the sail.

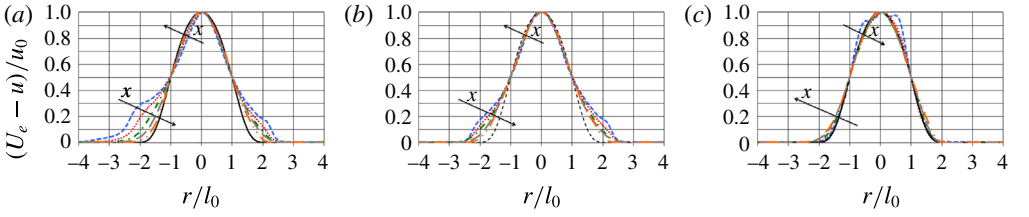

FIGURE 24. (Colour online) Time-averaged velocity defects in self-similar coordinates along the directions *a* (*a*), *b* (*b*) and average between *c*1 and *c*2 (*c*). Evolution downstream at five streamwise distances from the stern tail: – – – 1*D*; · · · · · · 3*D*; — · — 5*D*; ———— 7*D*; — · · — 9*D*. —— (3.2). Note that positive radial coordinates refer to the side away from the sail.

In contrast, in the plane of the sail (direction *a*) the effects of both the wake of the sail (on the left, negative radii) and that of the fins (on both sides, positive and negative radii) are obvious, especially at the outer radii (around $|r/l_0| = 2$), where the momentum deficit is increased. Along the direction *b*, in the plane normal to that of the sail, the influence of its wake is missing and the profiles are symmetric.

In figure 22 it is also clear that the establishment of self-similarity in the wake is faster at the inner radii than at the outer ones. This is shown in a more quantitative way in figure 24, where the profiles in self-similar coordinates are plotted along the directions *a*, *b* and *c* at five different streamwise locations in each plot, up to nine diameters from the stern tail. Again, the self-similar solution by Jiménez *et al.* (2010*b*) for the axial symmetric body has been added. Along the directions *a* and *b* the development downstream is characterized by a decrease of the momentum deficit at the outer radii and an increase at the inner radii, towards the self-similar model. However, it is quite evident that this process is faster near the axis, as the tip flows from the fins tend to decay slower when compared with the junction flows from their root. Note that the behaviour along the direction *c* is different. Again, the evolution towards the model is faster at the inner radii, but the momentum deficit is decreasing near the axis and increasing away from it. At this azimuthal location, in the middle between the planes of the fins, the influence of the appendages is initially negligible, but it becomes stronger moving downstream, due to wake diffusion. In all plots in figure 24 it is obvious that the wake is still evolving, although its azimuthal gradients undergo a significant reduction over the considered range of streamwise distances, approaching a self-similar state very close to that suggested by Jiménez

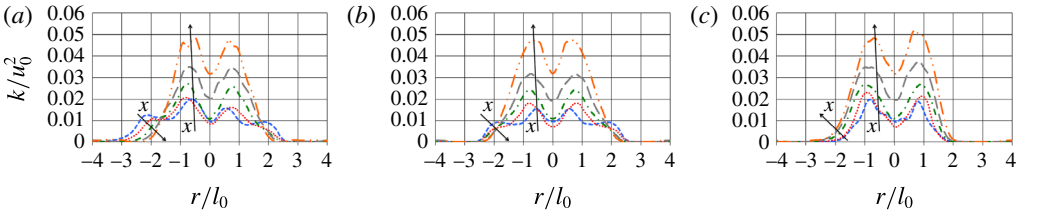

FIGURE 25. (Colour online) Profiles of turbulent kinetic energy in self-similar coordinates along the directions a (a), b (b) and average between $c1$ and $c2$ (c). Evolution downstream at five streamwise distances from the stern tail: – – – $1D$; · · · · · · $3D$; — · — $5D$; — — — $7D$; — · · — $9D$. Note that positive radial coordinates refer to the side away from the sail.

et al. (2010*b*) for the unappended DSub. We should note that the wake establishment is slower than that reported by Jiménez *et al.* (2010*a*) on the side away from the support of the unappended DSub. In the present case the overall wake is actually the overlap of the wake generated by the thick boundary layer developed along the stern and that of the appendages. The role of the fins is especially complex, and is characterized by additional momentum deficit in their wake, balanced at the inner radii by the opposite effect of their junction flows. In this sense the junction flows from the stern appendages shorten the delay in the development of the overall wake towards self-similarity, at least for the first-order statistics, as shown in figures 22 and 24.

Figure 25 shows the evolution of the profiles of turbulent kinetic energy, scaled in self-similar coordinates, at the same locations discussed in figure 24. In agreement with the results of the wind tunnel experiments by Jiménez *et al.* (2010*a*), the decay of turbulent kinetic energy is slower than that of momentum deficit, which implies an increase in self-similar coordinates. In all plots reported in figure 25 the dual peak associated with turbulence coming from the boundary layer over the stern is obvious, especially moving away from the body. It is also interesting to see that turbulence in the outer region of the SUBOFF wake in figure 25(*a*,*b*), tied to the wake of the appendages, both sail and fins, displays an opposite behaviour, decreasing at a higher rate than the momentum deficit: therefore the downstream profiles are narrower than the upstream ones. Note also that in the near wake, turbulence peaks are closer to the axis in the planes through the fins (figure 25*a*,*b*): this is caused by the junction flows, which increase turbulence levels near the stern surface. Moving downstream distributions become more symmetric and azimuthally uniform, although the evolution is not complete yet within the present streamwise extent: looking at figure 25 it is evident that at nine diameters from the tail of the submarine turbulence is far from self-similarity.

4. Conclusions

In the present work we report wall-resolved LES for the flow around an appended DSub model at the same conditions as in the experiment by Jiménez *et al.* (2010*b*) at $Re_L = 1.2 \times 10^6$. The level of numerical resolution utilized in the present computations goes beyond what has been reported in the literature today, resolving all essential flow features, including the turbulent boundary layers on the surface of the body. The accuracy of the computations was established by direct comparisons with the

experiments in the wake region. In the computations the geometry of the sail was the same as the original design by Groves *et al.* (1989), while in the experimental study a semi-infinite sail was used, in order to support the model. Our computations indicate that the influence of the sail wake is significantly reduced, compared with the experiments, due to its decreased extent. In particular, the momentum deficit associated with the shear layer from the sail is lower in the simulation, while in the same area downstream of the sail the normal stresses are decreased and the shear stresses are increased, in comparison with the wind tunnel measurements. Overall the instantaneous and time-averaged fields showed that in the DSub wake the main structures of the flow are associated with the tip of the fins and the thick boundary layer shed from the stern, whereas the sail wake has a rather limited influence moving downstream.

Details relative to the development of the boundary layer on the hull surface have been discussed, showing its significant acceleration and deceleration, along the bow and the stern, respectively, and the effects of its interaction with the appendages (both sail and fins). The effectiveness of the tripping strategy was verified, by comparison of the evolutions of the skin-friction coefficient, momentum thickness and shape factor, with those of a turbulent boundary layer on a flat plate under the effect of a zero pressure gradient. The hypothesis formulated by Jiménez *et al.* (2010*a*,*b*) about the origin of the bimodal behaviour of the wake, with a dual peak in the radial profiles of the stresses, has been confirmed, looking at the evolution of the boundary layer along the surface of the stern. The generation of an outer maximum of turbulence away from the surface of the body was observed under the effect of a strong adverse pressure gradient. Actually this phenomenon is due to a decrease of the turbulence in the buffer layer, while that in the outer layer is roughly unaffected. The wealth of information provided by the LES solution allowed us also to show that the stronger bimodal nature of the wake in the presence of appendages on the stern, found by Jiménez *et al.* (2010*b*), is attributable to the junctions flows developing at the root of the fins, increasing the velocity fluctuations in the boundary layer leaving the DSub surface. The same stern appendages are also responsible for azimuthal gradients of the momentum deficit and turbulence fields, with their consequent readjustment downstream towards a symmetric configuration.

The evolutions of the maximum velocity defect, u_0, and the half-wake width, l_0, proved to be roughly self-similar, at least on the side away from the sail, following power law trends in agreement with Jiménez *et al.* (2010*a*,*b*). However, the power laws describing the variation of u_0 and l_0 in the DSub wake are different from those in the above experiments, as they refer to the unappended geometry. This is consistent with the results reported in the literature, where the spreading rate of a self-similar wake depends on the wake generator (Ghosal & Rogers 1997; Johansson, George & Gourlay 2003; Ewing *et al.* 2007). Detailed analysis of the evolution of the time-averaged streamwise velocity defect in self-similar coordinates up to nine diameters from the tail and its comparison with the self-similar model by Jiménez *et al.* (2010*b*) for the unappended DSub showed that: (i) the evolution towards self-similarity is not complete yet at the last streamwise location, even for the first-order statistics, as the presence of the appendages delays significantly the development of the self-similar condition; (ii) this delay is stronger downstream of the tip of the fins, while the influence of the junction flows fades out more quickly in the DSub wake; (iii) the effect of the tip flows and the one of the junction flows are opposite, where they respectively increase and decrease the velocity defects; (iv) in the areas not affected by the wake of the appendages the numerical solution follows

closely the experimental self-similar model already at three diameters downstream of the body, which verifies the accuracy of the same model for the corresponding axial symmetric geometry (unappended DSub) and the quick attainment of self-similarity by its wake.

Acknowledgements

This work is supported by ONR Grant N000141110455, monitored by Dr K.-H. Kim. Computational time for this work is provided through an allocation from the DoD High Performance Computing Modernization Program.

REFERENCES

AKSELVOLL, K. & MOIN, P. 1996 An efficient method for temporal integration of the Navier–Stokes equations in confined axisymmetric geometries. *J. Comput. Phys.* **125** (2), 454–463.

ALIN, N., BENSOW, R. E., FUREBY, C., HUUVA, T. & SVENNBERG, U. 2010 Current capabilities of DES and LES for submarines at straight course. *J. Ship Res.* **54** (3), 184–196.

AUBERTINE, C. D. & EATON, J. K. 2005 Turbulence development in a non-equilibrium turbulent boundary layer with mild adverse pressure gradient. *J. Fluid Mech.* **532**, 345–364.

BALARAS, E. 2004 Modeling complex boundaries using an external force field on fixed Cartesian grids in large-eddy simulations. *Comput. Fluids* **33** (3), 375–404.

BALARAS, E., SCHROEDER, S. & POSA, A. 2015 Large-eddy simulations of submarine propellers. *J. Ship Res.* **59** (4), 227–237.

BERATLIS, N., SQUIRES, K. & BALARAS, E. 2012 Numerical investigation of Magnus effect on dimpled spheres. *J. Turbul.* **13**, 1–15.

BHUSHAN, S., ALAM, M. F. & WALTERS, D. K. 2013 Evaluation of hybrid RANS/LES models for prediction of flow around surface combatant and Suboff geometries. *Comput. Fluids* **88**, 834–849.

BOGER, D. A. & DREYER, J. J. 2006 Prediction of hydrodynamic forces and moments for underwater vehicles using overset grids. In *Proceedings of the 44th AIAA Aerospace Sciences Meeting and Exhibit, Reno, NV, USA, 9–12 January 2006*.

CHASE, N. & CARRICA, P. M. 2013 Submarine propeller computations and application to self-propulsion of DARPA Suboff. *Ocean Engng* **60**, 68–80.

CHASE, N., MICHAEL, T. & CARRICA, P. M. 2013 Overset simulation of a submarine and propeller in towed, self-propelled and maneuvering conditions. *Intl Shipbuilding Prog.* **60** (1–4), 171–205.

DEGRAAFF, D. B. & EATON, J. K. 2000 Reynolds-number scaling of the flat-plate turbulent boundary layer. *J. Fluid Mech.* **422**, 319–346.

EWING, D., GEORGE, W. K., ROGERS, M. M. & MOSER, R. D. 2007 Two-point similarity in temporally evolving plane wakes. *J. Fluid Mech.* **577**, 287–307.

GALPERIN, B. 1993 *Large Eddy Simulation of Complex Engineering and Geophysical Flows*. Cambridge University Press.

GEORGIADIS, N. J., RIZZETTA, D. P. & FUREBY, C. 2010 Large-eddy simulation: current capabilities, recommended practices, and future research. *AIAA J.* **48** (8), 1772–1784.

GHOSAL, S. & ROGERS, M. M. 1997 A numerical study of self-similarity in a turbulent plane wake using large-eddy simulation. *Phys. Fluids* **9** (6), 1729–1739.

GIVLER, R. C., GARTLING, D. K., ENGELMAN, M. S. & HAROUTUNIAN, V. 1991 Navier–Stokes simulations of flow past three-dimensional submarine models. *Comput. Meth. Appl. Mech. Engng* **87** (2–3), 175–200.

GORSKI, J. J., COLEMAN, R. M. & HAUSSLING, H. J. 1990 Computation of incompressible flow around the DARPA SUBOFF bodies. *Tech. Rep. No.* DTRC-90/016, David Taylor Research Center, Bethesda, MD.

GROVES, N. C., HUANG, T. T. & CHANG, M. S. 1989 Geometric characteristics of the DARPA SUBOFF models. *Tech. Rep. No.* DTRC/SHD-1298-01, David Taylor Research Center, Bethesda, MD.

HUANG, T., LIU, H. L., GROVES, N., FORLINI, T., BLANTON, J. & GOWING, S. 1994 Measurements of flows over an axisymmetric body with various appendages in a wind tunnel: the DARPA SUBOFF experimental program. In *Proceedings of the 19th Symposium on Naval Hydrodynamics, Seoul, Korea, 23–28 August 1992*, National Academy Press.

HUNT, J. C. R., WRAY, A. A. & MOIN, P. 1988 Eddies, stream, and convergence zones in turbulent flows. *Tech. Rep.* CTR-S88. Center for Turbulence Research Report.

JIMÉNEZ, J. M., HULTMARK, M. & SMITS, A. J. 2010*a* The intermediate wake of a body of revolution at high Reynolds numbers. *J. Fluid Mech.* **659**, 516–539.

JIMÉNEZ, J. M., REYNOLDS, R. T. & SMITS, A. J. 2010*b* The effects of fins on the intermediate wake of a submarine model. *ASME J. Fluids Eng.* **132** (3), 031102.

JOHANSSON, P. B. V., GEORGE, W. K. & GOURLAY, M. J. 2003 Equilibrium similarity, effects of initial conditions and local Reynolds number on the axisymmetric wake. *Phys. Fluids* **15** (3), 603–617.

LEE, J.-H. & SUNG, H. J. 2008 Effects of an adverse pressure gradient on a turbulent boundary layer. *Intl J. Heat Fluid Flow* **29** (3), 568–578.

MENEVEAU, C., LUND, T. S. & CABOT, W. H. 1996 A Lagrangian dynamic subgrid-scale model of turbulence. *J. Fluid Mech.* **319**, 353–385.

MERZ, R. A., YI, C. H. & PRZIREMBEL, C. E. G. 1986 Turbulence intensities in the near-wake of a semielliptical afterbody. *AIAA J.* **24** (12), 2038–2040.

MONTY, J. P., HARUN, Z. & MARUSIC, I. 2011 A parametric study of adverse pressure gradient turbulent boundary layers. *Intl J. Heat Fluid Flow* **32** (3), 575–585.

NICOUD, F. & DUCROS, F. 1999 Subgrid-scale stress modelling based on the square of the velocity gradient tensor. *Flow Turbul. Combust.* **62** (3), 183–200.

ORLANSKI, I. 1976 A simple boundary condition for unbounded hyperbolic flows. *J. Comput. Phys.* **21** (3), 251–269.

PATEL, V. C., NAKAYAMA, A. & DAMIAN, R. 1974 Measurements in the thick axisymmetric turbulent boundary layer near the tail of a body of revolution. *J. Fluid Mech.* **63**, 345–367.

PHILLIPS, A. B., TURNOCK, S. R. & FURLONG, M. 2010 Influence of turbulence closure models on the vortical flow field around a submarine body undergoing steady drift. *J. Mar. Sci. Technol.* **15** (3), 201–217.

POSA, A. & BALARAS, E. 2014 Model-based near-wall reconstructions for immersed-boundary methods. *Theor. Comp. Fluid Dyn.* **28** (4), 473–483.

POSA, A., LIPPOLIS, A. & BALARAS, E. 2015 Large-eddy simulation of a mixed-flow pump at off-design conditions. *ASME J. Fluids Eng.* **137** (10), 101302.

POSA, A., LIPPOLIS, A., VERZICCO, R. & BALARAS, E. 2011 Large-eddy simulations in mixed-flow pumps using an immersed-boundary method. *Comput. Fluids* **47** (1), 33–43.

SCHLICHTING, H. 1968 *Boundary-Layer Theory*. vol. 539. McGraw-Hill.

SKÅRE, P. E. & KROGSTAD, P.-Å. 1994 A turbulent equilibrium boundary layer near separation. *J. Fluid Mech.* **272**, 319–348.

SMITH, C. E., BERATLIS, N., BALARAS, E., SQUIRES, K. & TSUNODA, M. 2010 Numerical investigation of the flow over a golf ball in the subcritical and supercritical regimes. *Intl J. Heat Fluid Flow* **31** (3), 262–273.

SONG, S. & EATON, J. K. 2004 Reynolds number effects on a turbulent boundary layer with separation, reattachment, and recovery. *Exp. Fluids* **36** (2), 246–258.

SPALART, P. R. & WATMUFF, J. H. 1993 Experimental and numerical study of a turbulent boundary layer with pressure gradients. *J. Fluid Mech.* **249**, 337–371.

SPALART, P. R. 1988 Direct simulation of a turbulent boundary layer up to $Re_\theta = 1410$. *J. Fluid Mech.* **187**, 61–98.

SPALART, P. R., DECK, S., SHUR, M. L., SQUIRES, K. D., STRELETS, M. K. & TRAVIN, A. 2006 A new version of detached-eddy simulation, resistant to ambiguous grid densities. *Theor. Comp. Fluid Dyn.* **20** (3), 181–195.

SWARZTRAUBER, P. N. 1974 A direct method for the discrete solution of separable elliptic equations. *SIAM J. Numer. Anal.* **11** (6), 1136–1150.

TAYLOR, L. K., PANKAJAKSHAN, R., JIANG, M., SHENG, C., BRILEY, W. R., WHITFIELD, D. L., DAVOUDZADEH, F., BOGER, D. A., GIBELING, H. J., GORSKI, J., HAUSSLING, H., COLEMAN, R. & BULEY, G. 1998 Large-scale simulations for maneuvering submarines and propulsors. In *Proceedings of the 29th AIAA Plasmadynamics and Lasers Conference, Albuquerque, NM, USA, 15–18 June 1998*.

TOWNSEND, A. A. 1956 *The Structure of Turbulent Shear Flow*. Cambridge University Press.

VANELLA, M., POSA, A. & BALARAS, E. 2014 Adaptive mesh refinement for immersed boundary methods. *ASME J. Fluids Engng* **136** (4), 040909.

VAN KAN, J. J. I. M. 1986 A second-order accurate pressure-correction scheme for viscous incompressible flow. *SIAM J. Sci. Stat. Comput.* **7** (3), 870–891.

VAZ, G., TOXOPEUS, S. & HOLMES, S. 2010 Calculation of manoeuvring forces on submarines using two viscous-flow solvers. In *Proceedings of the 29th International Conference on Ocean, Offshore and Arctic Engineering, Shanghai, China, 6–11 June 2010*, ASME.

VERZICCO, R. & ORLANDI, P. 1996 A finite-difference scheme for three-dimensional incompressible flows in cylindrical coordinates. *J. Comput. Phys.* **123** (2), 402–414.

YANG, J. & BALARAS, E. 2006 An embedded-boundary formulation for large-eddy simulation of turbulent flows interacting with moving boundaries. *J. Comput. Phys.* **215** (1), 12–40.

ZHIHUA, L., YING, X. & CHENGXU, T. 2011 Numerical simulation and control of horseshoe vortex around an appendage-body junction. *J. Fluids Struct.* **27** (1), 23–42.

ZHIHUA, L., YING, X. & CHENGXU, T. 2012 Method to control unsteady force of submarine propeller based on the control of horseshoe vortex. *J. Ship Res.* **56** (1), 12–22.